Electronic Supplementary Information

White-emitting organometallo-silica nanoparticles for sunlike light-emitting diodes

C. Ezquerro,[a] E. Fresta,[b] E. Serrano,[c] E. Lalinde,[a] J. García-Martínez,*[c] J. R. Berenguer,*[a] R. D. Costa*[b]

Table of Contents

1. Experimental Procedures

General methods

Complexes **B** and **R** have been characterized by elemental analyses, mass spectrometry and the usual spectroscopic means (IR, Vis/UV, multinuclear NMR). Their emissive properties have been studied on a Jobin-Yvon Horiba Fluorolog 3-11 Tau-3 spectrofluorometer. All the reactions carried out to obtain complexes **B**, **G** and **R** were performed under Argon atmosphere and anhydrous conditions. $[Ir(ppy)_2(MeCN)_2]OTf,$[1] $[Ir(dfppy)_2(MeCN)_2]PF_6$[2] [ppy = 2-phenylpyridinyl; dfppy = 2-(2,4-difluorophenyl)pyridinyl] and ligand 4,4'-$[CONH(CH_2)_3Si(OEt)_3]$-bipiridine (dasipy)[3] were prepared as reported and other reagents were obtained from commercial sources and used without further purification. $[Ir(ppy)_2(PPETS)_2]OTf$ [**G**, PPETS = $PPh_2(CH_2)_2Si(OEt)_3$] preparation has already been reported.[4]

For a successful characterization of all the organometallo-silica materials, the NP suspensions were previously centrifuged at room temperature. The incorporation of the coordination compounds **B**, **G** and **R** in the organometallo-silica hybrid nanoparticles was evaluated by DRUV, FTIR spectroscopy techniques, and metal contents were determined by high resolution inductively coupled plasma mass spectrometry (HR-ICP-MS, ELEMENT XR). For this purpose, the samples were dissolved in a mixture of 3,5 ml HCl + 1 ml HNO_3 + 1 mL HF + 5mL H_3BO_3 (5%), digested in a microwave (260°C, 45 bar) and filtered off (0.45 μm) prior to analysis. This treatment is able to entirely dissolve the samples. The morphology of the mesoporous materials was investigated by transmission electron microscopy (TEM) and scanning electron microscopy (SEM). Both electron diffraction experiments and TEM images were performed using a JEM-2010 microscope (JEOL, 0.14 nm of resolution), at an accelerating voltage of 200 kV. Samples for TEM and FESEM studies were prepared by dipping a sonicated suspension of the sample in ethanol on a carbon-coated copper. The digital analysis of the TEM micrographs was performed using DigitalMicrographTM 3.6.1. by Gatan. SEM analyses were carried out in a field emission scanning electron microscope (FESEM) Merlin VP Compact (Zeiss, 1.6 nm of resolution at 1 kV). Porous texture was characterized by nitrogen sorption measurements at 77 K in an AUTOSORB-6 apparatus. The samples were previously degassed at 373 K for 8 h and 5×10^{-5} bars. Adsorption data were analysed using the software QuadraWinTM (version 6.0) of Quantachrome Instruments. The BET surface area was estimated by using multipoint BET method, using the adsorption data in the relative pressure (P/P_0) range of 0.05–0.25. Pore-size distribution curves were calculated using the DFT method (NLDFT equilibrium model, which assumes nitrogen adsorption at 77 K in cylindrical

silica pores for the mesopore range). The total pore volume and the mesopore volume were read directly from the adsorption branch of the isotherm at 0.8 and 0.99, respectively (the micropore volume was determined by using t-plot method to be 0).

Full equipment and experimental conditions used have been described elsewhere.[4] Fig. S1 shows the numbering scheme used in the NMR characterization.
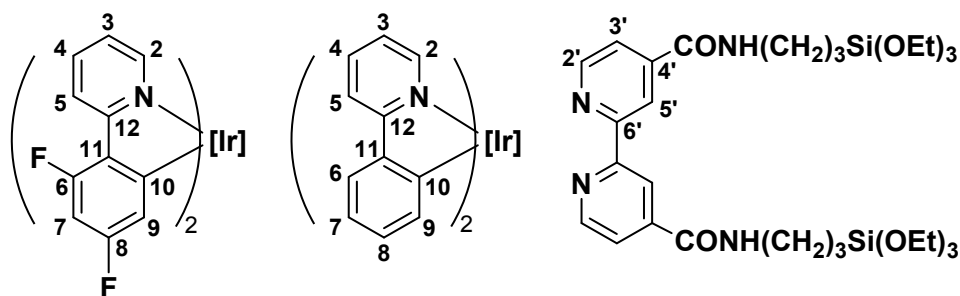

Figure S1. Chemical structures of the complexes highlighting the numbering used in the NMR.

Synthetic methods

Synthesis of [Ir(dfppy)$_2$(PPETS)$_2$]PF$_6$ (B). A yellow solution of 0.2 g (0.25 mmol) of [Ir(dfppy)$_2$(MeCN)$_2$]PF$_6$ in 20 ml of dichloromethane was treated with 312 μl (0.87 mmol) of PPETS. The yellow mixture was stirred for 48h and the resulting solution was evaporated to dryness. Treatment of the residue with hexane yielded compound **B** as a pale-yellow solid (0.26 g, 71%). Anal. Calc. for C$_{62}$F$_{10}$H$_{70}$IrN$_2$O$_6$P$_3$Si$_2$: C, 50.60; H, 4.79; N, 1.90. Found: C, 50.64; H, 4.36; N, 1.74. ESI (+): $^m/_z$ 1325 [M]$^+$ (100%); 949 [M–PPETS]$^+$ (13%). IR (KBr, cm^{-1}): ν(C-H) 3069 (m), 2970 (s), 2925 (m), 2890 (m); ν(ring) 1603 (vs), 1576(vs), 1480(vs); ν(P-C) 1430 (vs); ν(ring) 1405(vs); ν(C-F) 1254 (s); δ(C-H)+ν(ring) 1296(s); 1164(vs); ν(Si-O-C) 1102 (vs), 1080 (vs); ν(P-F) 842 (vs). ^{1}H NMR (400 MHz, CDCl$_3$, δ): 8.75 (d, J_{H-H} = 6.2 Hz, 2H, H^2); 7.94 (d, J_{H-H} = 8.1 Hz, 2H, H^5); 7.76 (t, J_{H-H} = 7.9 Hz, 2H, H^4); 7.38-7.28 (m, 8H, o-Ph); 7.14 (psc, J_{H-H} = 8.3 Hz, 8H, m-Ph); 7.0 (t, J_{H-H} = 6.6 Hz, 2H, H^3); 6.70 (t, J_{H-H} = 8.3 Hz, 4H, p-Ph); 6.51 (pst, J_{H-H} = 10.3 Hz, 2H, H^7); 5.20 (d, J_{H-H} = 9.3 Hz, 2H, H^9); 3.58 (c, J_{H-H} = 6.7 Hz, 12H, OCH_2CH$_3$); 2.11 (m, 2H, PCH_2CH$_2$Si); 1.88 (m, 2H, PCH_2CH$_2$Si); 1.05 (t, J_{H-H} = 6.9 Hz, 18H, OCH$_2$CH_3); 0.21 (m, 2H, PCH$_2$CH_2Si); 0.05 (m, 2H, PCH$_2$CH_2Si). ^{13}C{^{1}H} NMR (100.6 MHz, CDCl$_3$, δ): 164.2 (s, C^{12}); 161.7 (s broad, C^8); 159.9 (s broad, C^6); 155.0 (s, C^2); 139.2 (s, C^4); 134.3 (t, $^2J_{P-C}$ = 5.3 Hz, o-Ph); 131.8 (t, $^2J_{P-C}$ = 3.5 Hz, o-Ph); 131.5 (s, p-Ph); 130.4 (s, p-Ph); 128.8-128.4 (m broad, m-Ph and probably ipso-C); 127.9 (s, C^{11}); ~125 (ipso-C); 123.8 (s, C^5); 122.5 (s, C^3); 113.7 (d, $^2J_{F-C}$ = 18.5 Hz, C^9); 100.0 (pst, $^{2+2}J_{F-C}$ = 26.8 HZ, C^7); 58.4 (s, OCH$_2$CH$_3$); 19.3 (m, PCH$_2$CH$_2$Si); 18.3 (m,

3

PCH_2CH$_2$Si); 17.7 (s, OCH$_2$$CH_3$); 4.6 (m, PCH$_2$$CH_2$Si). ^{31}P{^{1}H} NMR (162.1 MHz, CDCl$_3$, δ): -144.4 (sp, J$_{P-F}$ = 712 Hz, PF_6); -8.89 (s, PPh$_2$). ^{19}F{^{1}H} NMR (376.5 MHz, CDCl$_3$, δ): -73.2 (d, J$_{P-F}$ = 712 Hz, PF_6); -104.5 (d, J = 9.4 Hz, F^6); -107.7 (d, J = 8.8 Hz, F^8).

Synthesis of [Ir(ppy)$_2$(dasipy)]OTf (R). The addition of 0.18 g (0.27 mmol) of dasipy to a yellow solution of 0.20 g (0.27 mmol) of [Ir(ppy)$_2$(CH$_3$CN)$_2$]OTf in 30 ml of dichloromethane gave a red solution, which was stirred for 2h at r.t. The mixture was evaporated to dryness. The final solid (**R**) was kept under Ar atmosphere (0.27 g, 77%). Anal. Calc. for C$_{53}$F$_3$H$_{66}$IrN$_6$O$_{11}$SSi$_2$: C, 48.91; H, 5.12; N, 6.46; S, 2.46. Found: C, 48.88; H, 4.66; N, 7.28; S, 3.94. ESI (+): $^m/_z$ 1151 [M]$^+$ (100%). IR (KBr, cm^{-1}): ν(N-H) 3315 (m); ν(C-H) 3062 (m), 2974 (m), 2924 (m), 2874 (m); ν(C=O) 1669 (vs); ν(ring) 1608 (s), 1583 (s), 1550 (vs), 1479 (vs), 1439 (m), 1419 (m); ν(Si-O-C) 1164 (vs), 1069 (vs); ν(S-O) 1403 (m), 1031 (vs). ^{1}H NMR (400 MHz, CDCl$_3$, δ): 9.11 (s broad, 2H, H$^{5'}$); 8.69 (s broad, 2H, NH); 8.04 (d, J$_{H-H}$ = 5.6 Hz, 2H, H$^{2'}$ or H$^{3'}$); 7.94 (m, 4H, 2H^2, 2H$^{2'}$ or 2H$^{3'}$); 7.78 (t, J$_{H-H}$ = 7.6 Hz, 2H, H^3); 7.70 (d, J$_{H-H}$ = 7.7 Hz, 2H, H^6); 7.46 (d, J$_{H-H}$ = 5.6 Hz, 2H, H^5); 7.07 (t, J$_{H-H}$ = 7.4 Hz, 2H, H^7), 7.00 (t, J$_{H-H}$ = 6.5 Hz, 2H, H^4); 6.94 (t, J$_{H-H}$ = 7.3 Hz, 2H, H^8); 6.28 (d, J$_{H-H}$ = 7.5 Hz, 2H, H^9); 3.81 (c, J$_{H-H}$ = 7.0 Hz, 12H, OCH_2CH$_3$); 3.47 (m, 4H, CH_2CH$_2$CH$_2$Si); 1.79 (m, 4H, CH$_2$$CH_2CH_2$Si); 1.21 (t, J$_{H-H}$ = 7.0 Hz, 18H, OCH$_2$$CH_3$); 0.70 (t, J$_{H-H}$ = 8.4 Hz, 4H, CH$_2$CH$_2$$CH_2$Si). ^{13}C{^{1}H} NMR (100.6 MHz, CDCl$_3$, δ): 167.9 (s, C^{12}); 163.7 (s, CO); 156.0 (s, C$^{4'}$or C$^{6'}$); 151.0 (s, C$^{2'}$ or C$^{3'}$); 149.9 (s, C^{10}); 148.5 (s, C^5); 146.0 (s, C$^{4'}$or C^6); 143.4 (s, C^{11}); 138.4 (s, C^3); 131.8 (s, C^9); 131.2 (s, C^8); 128.0 (s, C$^{2'}$or C$^{3'}$); 125.1 (s, C^6); 123.5 (s, C^4); 123.1 (s, C^7); 122.4 (s, C$^{5'}$); 119.9 (s, C^2); 58.5 (s, OCH_2CH$_3$); 43.5 (s, CH_2CH$_2$CH$_2$Si); 22.7 (s, CH$_2$$CH_2CH_2$Si); 18.4 (s, OCH$_2$$CH_3$); 8.0 (s, CH$_2CH_2$$CH_2$Si). ^{19}F{^{1}H} NMR (376.5 MHz, CDCl$_3$, δ): -78.0 (s).

Synthesis of luminescent mesoporous organometallo-silica nanoparticles (NP_B,G,R). Monochromatic **NP_B,G,R** nanoparticles were obtained by co-condensation of the corresponding complexes (**B**,**G**,**R**) with the silica precursor (TEOS), in the presence of a cationic surfactant (cetyltrimethylammonium bromide, CTAB). In a typical synthesis, a solution of the respective complexes (8 mg, 0.006 mmol **B**; 8 mg, 0.006 mmol **G** or 7 mg, 0.006 mmol **R**) in 3 ml of absolute ethanol was added dropwise to a solution of 0.20 g (0.55 mmol) of CTAB and 31.4 μl (0.24 mmol) of triethanolamine (TEA) in 13.3 ml (0.74 mmol) of distilled water. The mixture was kept under magnetic stirring for 6 (for **B** and **G**) or 2 hours (for **R**) to form the corresponding monochromatic emitting organometallic dots (**OD_B**, **OD_G**, **OD_R**). Then, a solution of 2 ml (9.12 mmol) of TEOS in 1ml of absolute ethanol was added dropwise to the mixture and stirred at r.t. for 24 hours. The resulting suspension was centrifuged (20000 r.p.m., 20 minutes)

4

and washed with ethanol. In order to remove the surfactant, exchange with ammonium nitrate (10 mg/ml) was carried out. The materials were obtained as pale yellow (**NP_B** and **NP_G**) and pale orange (**NP_R**) solids. The molar ratio of the synthesis gel is the following: 1.0 TEOS:0.06 CTAB:0.026 TEA:80 H_2O, being the nominal iridium metal concentration 0.2 wt.%. See Scheme S1 for a schematic representation of the synthesis of the blue-emitting organometallic nanoparticles (**NP_B**). **NP_B** (0.41 g, 73%). IR (KBr, cm^{-1}): ν(O-H) 3475 (s broad), 1640 (m); ν(C-H) 2980 (vw), 2925 (w), 2854 (w); ν(ring) 1487 (w), 1401(w), 1380(w); ν(Si-O-Si) 1220, 1080 (vs broad), 800 (m), 460 (s); ν(Si-O) 950 (m). DRUV (KBr): λ_{max} 230, 240, 260, 297, 312, 350. **NP_G** (0.38 g, 69%). IR (KBr, cm^{-1}): ν(O-H) 3450 (s broad), 1633 (m); ν(C-H) 2980 (vw), 2924 (m), 2851 (m); ν(ring) 1490 (w), 1478(w), 1457(w), 1383(w); ν(Si-O-Si) 1220, 1080 (s broad), 800 (m), 460 (s); ν(Si-O) 940 (s). DRUV (KBr): λ_{max} 240, 264, 314, 362. **NP_R** (0.38 g, 69%). IR (KBr, cm^{-1}): ν(O-H) 3450 (s broad), 1630 (m); ν(C-H) 2925 (m), 2855 (m); ν(ring) 1560 (vw), 1540(vw), 1475(vw); ν(Si-O-Si) 1220, 1080 (vs broad), 800 (m), 460 (s); ν(Si-O) 950 (m). DRUV (KBr): λ_{max} 224, 238, 272, 294, 310, 372, 467, 494.

Synthesis of mesoporous organometallo-free silica nanoparticles (Control NP). Complex-free mesoporous silica nanoparticles (**Control NP**) were prepared following the same procedure described for the monochromatic **NP_B,G,R** nanoparticles without adding the metal complexes.

Synthesis of white emissive mesoporous organometallo-silica nanoparticles (NP_W). **NP_W** nanoparticles were prepared following a similar approach to that described for the monochromatic **NP_B,G,R** nanoparticles. A solution of a mixture of complexes **B** and **G** (5.25 mg, 0.004 mmol **B** and 2.25 mg, 0.002 mmol **G**) in 2 ml of absolute ethanol was added dropwise to the starting solution of CTAB, TEA and distilled water. The mixture was stirred for 4 hours at room temperature. Then, a solution of complex **R** (0.4 mg, 0.0003 mmol) in 1 ml of EtOH was added dropwise and the mixture stirred for 2 more hours to form the white emitting organometallic dots **OD_W**. The following procedure was the same as that described before for the synthesis of the monochromatic **NP_B,G,R** nanoparticles. The total nominal iridium metal content was also 0.2 wt.% (0.125 wt.% **B**; 0.064 wt.% **G** and 0.011 wt.% **R**), and the molar ratio of the synthesis gel is the same than that for **NP_B,G,R**. **NP_W** (0.30 g, 54%). IR (KBr, cm^{-1}): ν(O-H) 3465 (s broad), 1638 (w); ν(C-H) 2956(w), 2925 (m), 2854 (m); ν(ring)

1559 (w), 1540 (w), 1506(w), 1489(w), 1456(w); ν(Si-O-Si) 1220, 1084 (vs broad), 800 (mw), 460 (sm); ν(Si-O) 950 (s). DRUV (KBr): λ_{max} 246, 258, 268, 298, 311, 358.

Several materials have been done by changing the relative amount of the three chromophores and maintaining the total nominal iridium metal content to 0.2 wt.%. Nevertheless, higher relative amounts of complex **R** produce nanoparticles which display overall red-visual emissions under UV/Vis illumination.

The same approach was followed to prepare materials with a total nominal metal concentration of 0.6 wt.% (0.375 wt.% **B**; 0.192 wt.% **G** and 0.033 wt.% **R**, **NP_W_0.6wt.%**) and 1 wt.% (0.625 wt.% **B**; 0.320 wt.% **G** and 0.055 wt.% **R**, **NP_W_1wt.%**). We tried the same molar ratio of the synthesis gels and also more diluted media (for instance 1.0 TEOS:0.18 CTAB:0.078 TEA:237.6 H_2O. **NP_W_0.6wt.%** Yield: 0.36 g, 63%. **NP_W_1wt%** Yield:0.41 g, 73%). In all cases, the materials are formed by aggregation of nanoparticles and not by discrete nanoparticles, showing lesser quantum yields (ca. 18%) than those observed for both **NP_B,G,R** and **NP_W.**
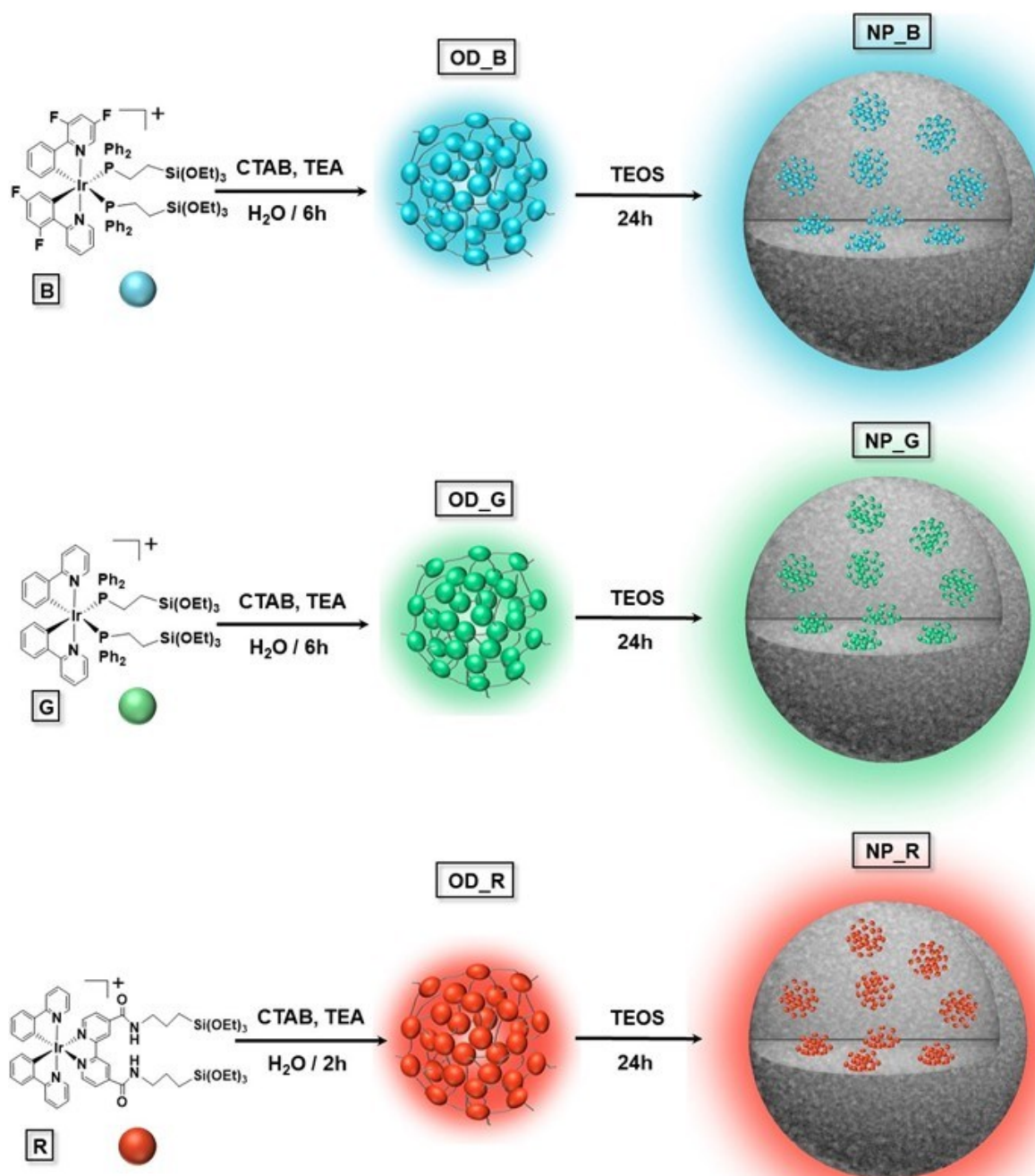
Scheme S1. Schematic representation of the synthesis of the monochromatic-emitting organometallic nanoparticles (**NP_B**,**G**,**R**) through the formation of their corresponding organometallic dots (**OD_B**,**G**,**R**).

2. Theoretical calculations

Calculations for complexes **B** and **R** were carried out with the Gaussian 09 package,[5] using Becke's three-parameter functional combined with Lee-Yang-Parr's correlation functional (B3LYP) in the singlet state (S_0) and the unrestricted U-B3LYP in the triplet state (T_1).[6] According to previous theoretical calculations for iridium complexes, the optimized ground state geometry were calculated at the B3LYP/LANL2DZ (Ir)/6-31G(d,p) (ligands' atoms) level. The S_0 geometry was found to be a true minimum as no negative frequencies in the vibrational frequency study of the final geometry were found. DFT and TD-DFT calculations were carried out using the polarized continuum model approach implemented in the Gaussian 09 software. The MO diagrams and the orbital contributions were generated with Gaussian 09 software and Gauss-Sum[7] program, respectively. The emission energy was calculated as the difference of the DFT-optimized T_1 geometry for both states (adiabatic electronic transition).

Table S1. DFT optimized geometries for ground state and triplet state of complexes **B** and **R.**

|	**B**			**R**	
	S_0	T_1		S_0	T_1
Ir(1)-N(1)	2.108	2.117	Ir(1)-N(1)	2.085	2.083
Ir(1)-N(1')	2.107	2.072	Ir(1)-N(1')	2.082	2.083
Ir(1)-C(10)	2.049	2.046	Ir(1)-C(10)	2.024	1.999
Ir(1)-C(10')	2.046	2.031	Ir(1)-C(10')	2.034	1.997
Ir(1)-P(1)	2.587	2.596	Ir(1)-N(a)	2.208	2.201
Ir(1)-P(1')	2.584	2.614	Ir(1)-N(a')	2.207	2.193
N(1)-Ir(1)-N(1')	167.26	168.28	N(1)-Ir(1)-N(1')	173.60	176.39
N(1)-Ir(1)-C(10)	79.03	79.09	N(1)-Ir(1)-C(10)	80.05	80.85
N(1')-Ir(1)-C(10')	79.15	80.49	N(1')-Ir(1)-C(10')	80.05	80.82
N(1)-Ir(1)-C(10')	91.92	91.69	N(a)-Ir(1)-N(a')	95.50	96.79
N(1')-Ir(1)-C(10)	90.98	91.49	N(1)-Ir(1)-C(10')	95.24	96.66
P(1)-Ir(1)-P(1')	100.10	100.08	N(1')-Ir(1)-C(10)	74.79	75.01
P(1)-Ir(1)-N(1)	85.56	85.61	N(a)-Ir(1)-N(1)	88.09	87.41
P(1)-Ir(1)-C(10)	87.72	87.58	N(a)-Ir(1)-C(10)	97.98	94.62
P(1)-Ir(1)-N(1')	102.07	101.09	N(a)-Ir(1)-N(1')	96.90	95.42
P(1)-Ir(1)-C(10')	172.13	172.74	N(a)-Ir(1)-C(10')	172.24	169.18
P(1')-Ir(1)-N(1)	104.16	104.10	N(a')-Ir(1)-N(1)	96.75	95.06
P(1')-Ir(1)-C(10)	171.71	171.85	N(a')-Ir(1)-C(10)	172.26	169.09
P(1')-Ir(1)-N(1')	84.72	84.35	N(a')-Ir(1)-N(1')	88.45	87.85
P(1')-Ir(1)-C(10')	87.75	87.12	N(a')-Ir(1)-C(10')	97.91	94.63
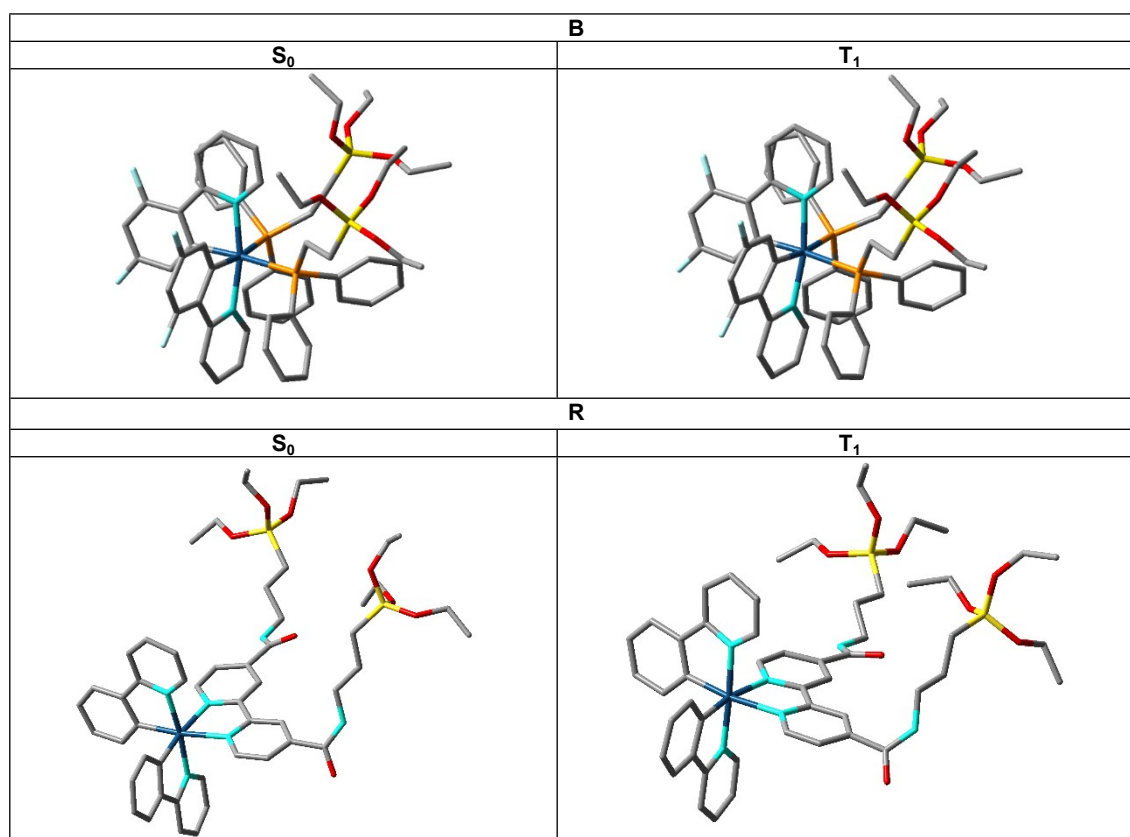
Figure S2. Optimized structures of S_0 and T_1 states of complexes **B** and **R**.

Table S2. Composition (%) of Frontier MOs in the ground state for complexes **B** and **R** in THF.

	B					**R**				
	eV	dFppy (1)	dFppy (2)	PPETS (1)	PPETS (2)	Ir	eV	ppy (1)	ppy (2)	dasipy	Ir
LUMO+5	-1.22	9	3	28	52	8	-1.42	35	58	5	2
LUMO+4	-1.34	10	6	55	23	6	-1.92	55	38	4	4
LUMO+3	-1.45	41	44	2	10	1	-2.01	38	57	1	4
LUMO+2	-1.57	40	50	2	6	1	-2.07	3	2	94	1
LUMO+1	-2.02	57	36	1	1	4	-2.18	1	2	96	1
LUMO	-2.17	36	58	2	2	2	-3.00	0	0	96	3
HOMO	-6.40	31	33	1	2	33	-5.89	31	30	2	38
HOMO-1	-6.60	48	42	3	2	5	-6.52	47	45	1	7
HOMO-2	-6.80	41	43	4	1	10	-6.68	31	30	3	35
HOMO-3	-6.83	20	22	12	40	5	-6.80	26	30	7	37
HOMO-4	-6.91	8	15	45	22	10	-6.87	31	24	4	40
HOMO-5	-7.13	24	24	17	30	6	-6.97	30	38	5	28
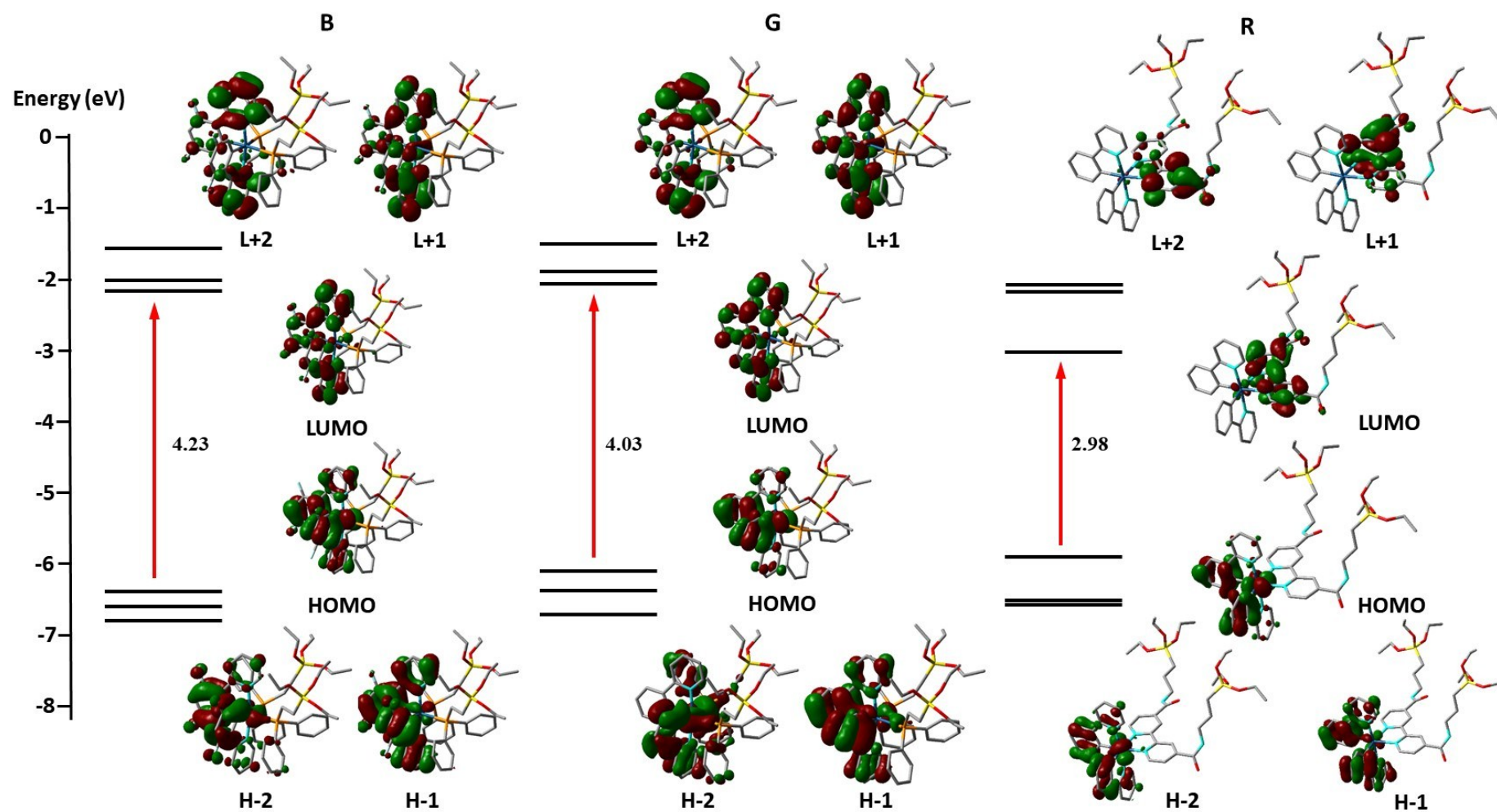
Figure S3. Selected frontier Molecular Orbitals for complexes **B**, **G** and **R**, showing the electronic gap between HOMO-LUMO orbitals (Data of **G** already published).[4]

Table S3. Selected vertical excitation energies singlets (S_0) and first triplets computed by TDDFT/SCRF (THF) with the orbitals involved for complexes for complexes **B** and **R**.

| State	λ_{ex}(calc)(nm)	f	Transition (% Contribution)	Main character
			B	
T_1	423.9	0.0	H-1→LUMO (11%), H-1→L+1 (17%), HOMO→LUMO (38%)	MLCT/IL
T_2	421.4	0.0	H-1→LUMO (29%), H-1→L+1 (11%), HOMO→L+1 (26%)	MLCT/IL
T_3	356.4	0.0	H-2→LUMO (23%), HOMO→LUMO (37%)	MLCT/IL
S_1	354.6	0.042	HOMO→LUMO (95%)	MLCT/IL
S_2	340.8	0.0034	HOMO→L+1 (94%)	MLCT/IL
S_3	323.3	0.0098	H-1→LUMO (88%)	IL
S_4	314.9	0.042	H-1→L+1 (85%)	IL
S_5	308.4	0.0539	H-2→LUMO (86%)	IL
S_6	306.1	0.0679	H-3→LUMO (87%)	L'LCT/IL
S_7	301.2	0.0502	H-4→LUMO (90%)	L'LCT
S_{35}	259.2	0.0683	H-3→L+3 (43%), HOMO→L+6 (15%)	L'LCT/IL
			R	
T_1	498.55	0.0	HOMO→LUMO (98%)	ML'CT/LL'CT
T_2	450.01	0.0	H-1→L+4 (15%), HOMO→L+3 (63%)	MLCT/IL
S_1	492.98	0.0004	HOMO→LUMO (99%)	ML'CT/LL'CT
S_2	419.27	0.0023	H-4→LUMO (25%), H-2→LUMO (71%)	ML'CT/LL'CT
S_3	415.33	0.0287	H-1→LUMO (93%)	LL'CT/ML'CT
S_5	396.57	0.0591	HOMO→L+3 (96%)	IL/MLCT
S_6	388.98	0.0757	H-3→LUMO (67%), HOMO→L+2 (12%)	ML'CT/LL'CT
S_8	377.12	0.0211	H-4→LUMO (11%), H-3→LUMO (11%), HOMO→L+2 (12%), HOMO→L+4 (58%)	ML'CT/LL'CT /IL/MLCT
S_{10}	360.74	0.0198	H-5→LUMO (88%), H-3→LUMO (10%)	ML'CT/LL'CT
S_{16}	320.35	0.0355	H-2→L+1 (19%), H-2→L+3 (12%), H-1→L+3 (35%)	IL/ML'CT/LL'CT
S_{31}	291.66	0.1186	H-4→L+2 (34%), H-4→L+3 (25%)	ML'CT/LL'CT/IL
S_{38}	285.52	0.2311	H-3→L+3 (14%), H-2→L+3 (13%), H-4→L+4 (10%)	IL/MLCT
S_{51}	266.37	0.3573	H-2→L+5 (10%), H-1→L+6 (46%), HOMO→L+8 (20%)	IL/MLCT
S_{60}	257.83	0.2280	H-3→L+6 (25%), HOMO→L+8 (37%)	IL/MLCT
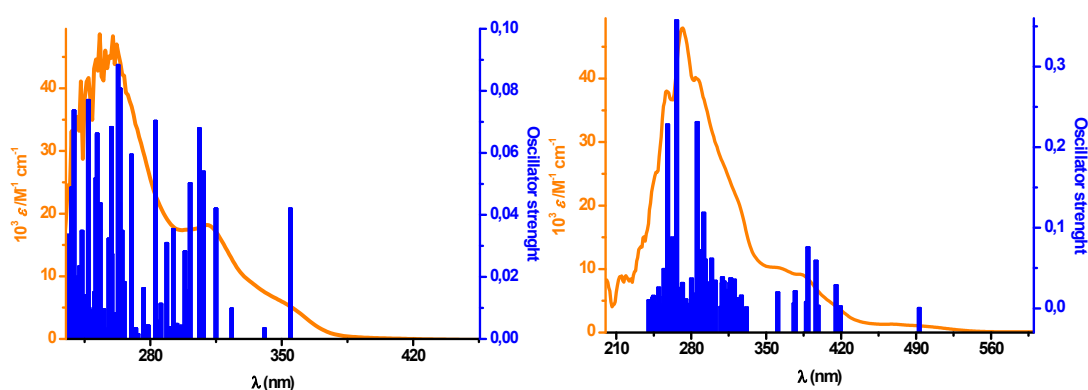
Figure S4. Calculated stick absorption spectra of complexes **B** (left) and **R** (right) in THF compared with the experimental one.

Table S4. Composition (%) of frontier molecular orbitals in the first triple-state for compound **B** and **R** in THF.

	1						3				
	eV	dFppy (1)	dFppy (2)	PPETS (1)	PPETS (2)	Ir	eV	ppy (1)	ppy (2)	dasipy	Ir
SOMO	-3.78	1	94	0	2	3	-3.84	0	0	98	2
SOMO-1	-4.87	1	89	0	1	9	-5.11	28	28	3	41
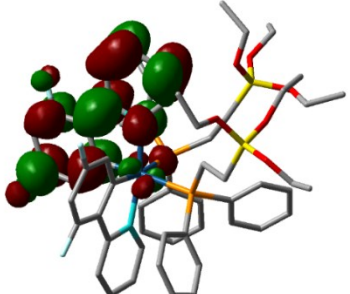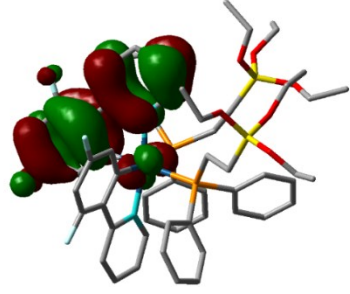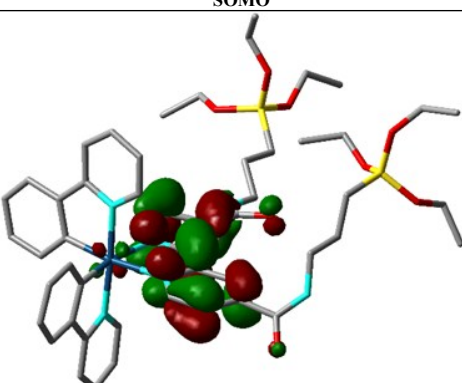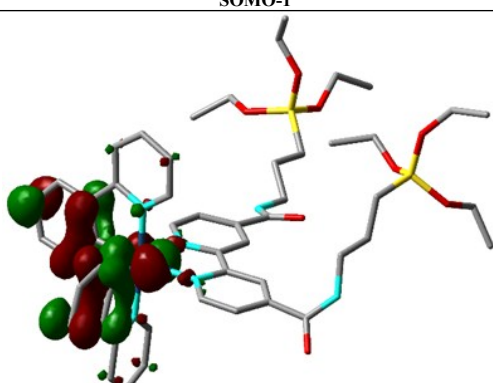
Figure S5. SOMO and SOMO-1 orbitals for complexes **B** and **R**.

Spin density: 0.109417   *Spin density: 0.496468*
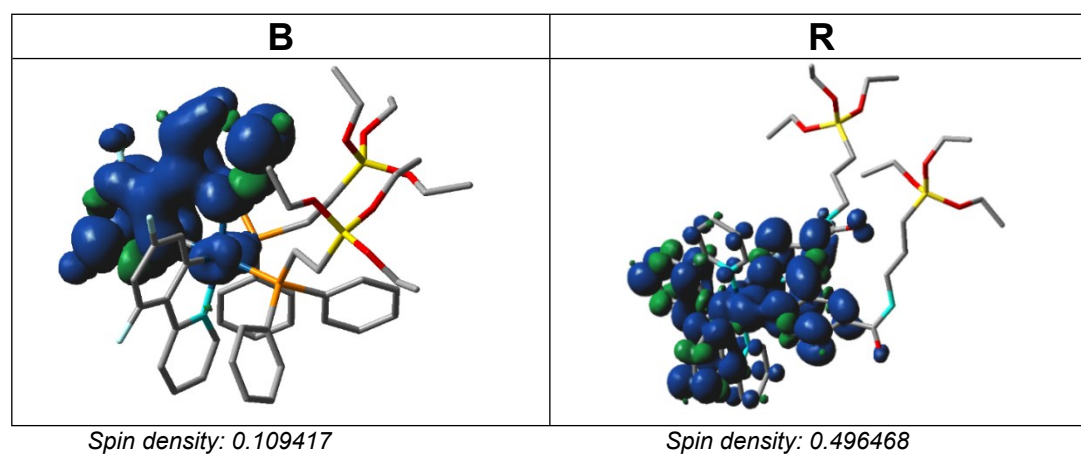
Figure S6. Spin-density distributions calculated for the emitting excited state (T$_1$) of complexes **B** and **R**.

3. Solid state emission spectra of B and G vs. DRUV spectrum of R
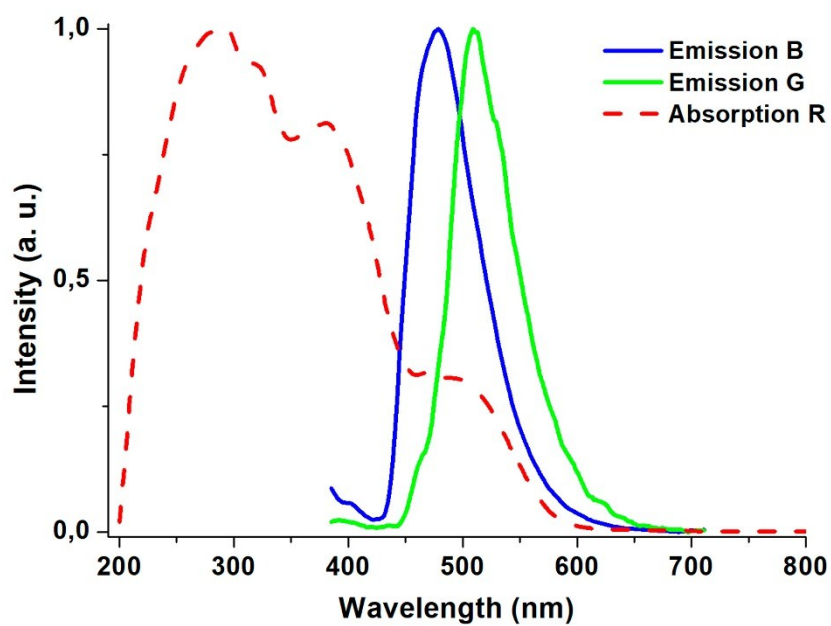
Figure S7. Solid state DRUV spectrum of complex **R** and emission spectra of complexes **B** and **G** (λ_{ex} 365 nm) in the solid state showing the overlapping in the zone of 450 – 550 nm.

4. Textural and morphological characterization

Table S5. Metal content and textural properties of the monochromatic **NP_B**,**G**,**R** and the white emitting **NP_W** organometallo-silica nanoparticles in comparison with the related complex-free control silica nanoparticles (**Control NP**).

Sample	$Ir^{a)}$ (wt.%)	$A_{BET}^{b)}$ (m^2/g)	$V_p^{0.8, c)}$ (cm^3/g)	$V_p^{0.99, d)}$ (cm^3/g)	$d_p^{e)}$ (nm)
Control NP	---	1070	0.61	1.3	2.4
NP_R	0.18 (0.20)	940	0.49	1.0	2.3
NP_G	0.18 (0.20)	990	0.56	1.2	2.3
NP_B	0.18 (0.20)	1154	0.67	1.4	2.1
NP_W	0.16 (0.20)	1032	0.58	1.5	2.1

a) Iridium content calculated from high resolution ICP mass spectroscopy analyses after treatment of the samples with diluted HF. Values in brackets represent the nominal metal content. b) BET surface area estimated by multipoint BET method using the adsorption data in the relative pressure (P/P_0) range of 0.05–0.25. (c) Mesopore volume read directly from the adsorption branch of the isotherm at (P/P_0) = 0.8. (d) Total pore volume read directly from the adsorption branch of the isotherm at 0.99. (e) Average mesopore diameter determined from the isotherm using the NLDFT equilibrium model. Samples were centrifuged and air dried before gas adsorption measurements.
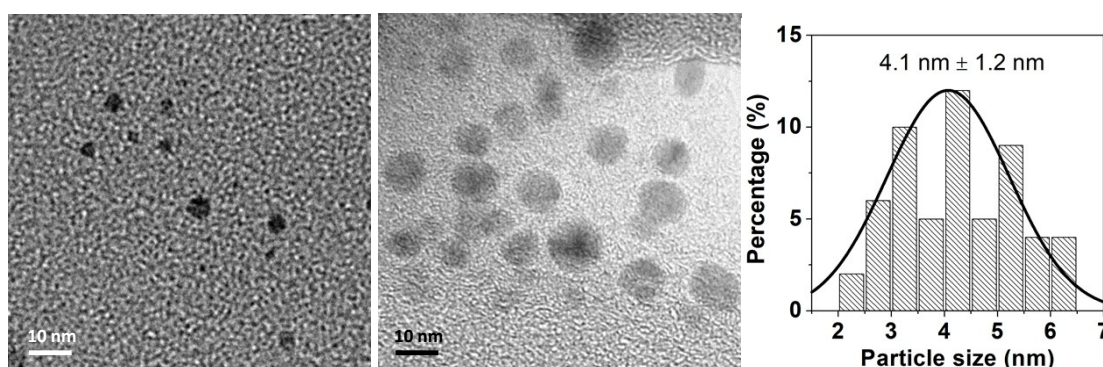

Figure S8. Representative TEM image of the monochromatic- **OD_R** (left) and the white-emitting **OD_W** (middle) organometallic dots, as well as the histogram showing the particle size distribution of **OD_W** (right).
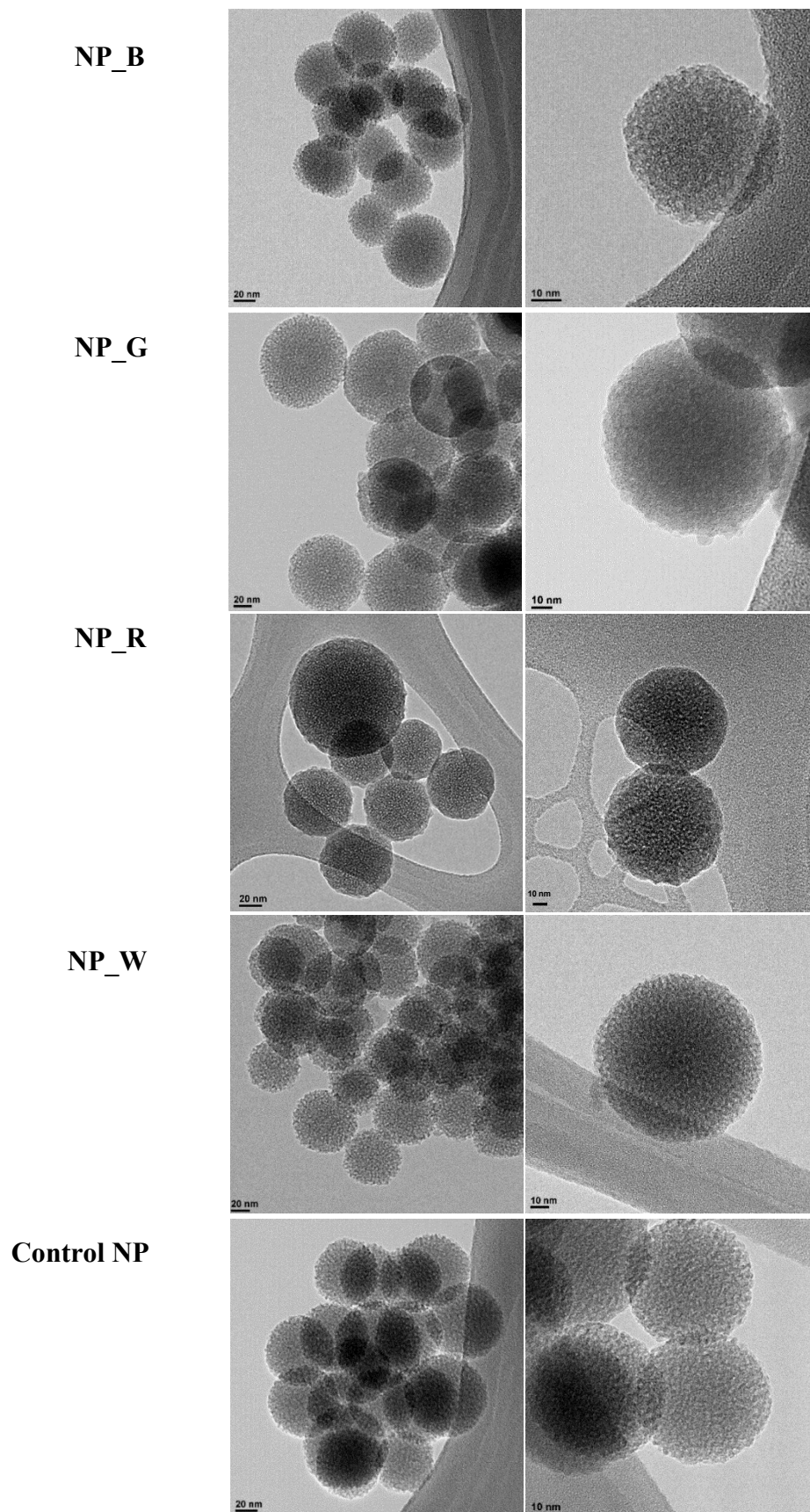
NP_B

NP_G

NP_R

NP_W

Control NP

Figure S9. TEM images of the monochromatic emitting **NP_B**,**G,R**, the white-emitting **NP_W** nanoparticles and the complex-free silica nanoparticles, **Control NP**.
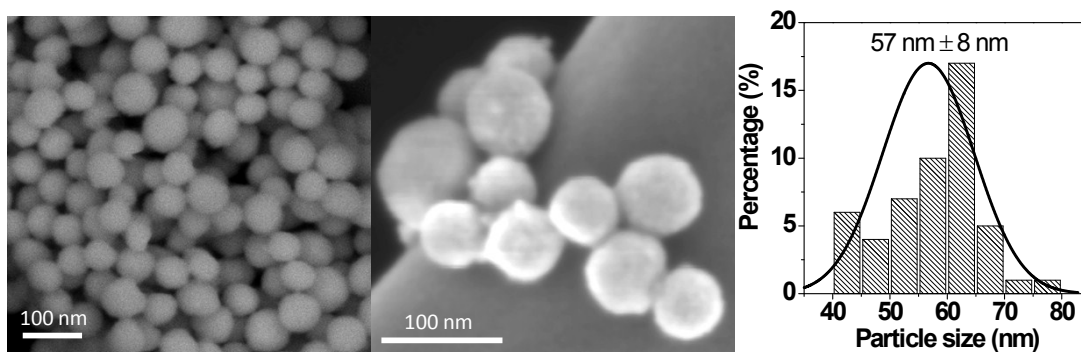
15

Figure S10. Representative FESEM images of the white-emitting organometallo-silica nanoparticles **NP_W** (left) and the corresponding histogram showing the particle size distribution (right).
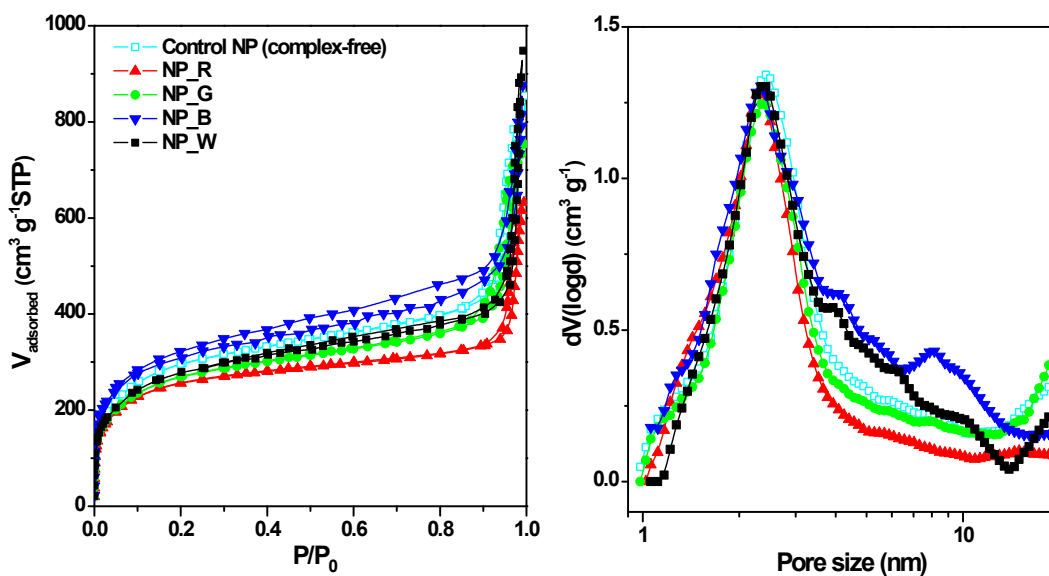

Figure S11. N_2 adsorption/desorption isotherms at 77K (left) and the corresponding pore size distribution calculated using the NLDFT method (right) of the monochromatic-**NP_B**,**G**,**R** and the white-emitting **NP_W** organometallo-silica nanoparticles in comparison with the related complex-free silica nanoparticles (**Control NP**).

5. Photophysical properties of pure complexes and nanoparticles.

The absorption and emission data of the precursors **B**, **G** and **R**, those of their corresponding organometallic dots in the reaction media (**OD_B, OD_G**, **OD_R** and **OD_W**), and the hybrid organometallo-silica nanoparticles (**NP_B, NP_G**, **NP_R** and **NP_W**) in different media are summarized in Tables S6 and S7. Some representative spectra are collected in Fig. 1 and Fig. S12–S19. TD-DFT calculations (THF solution and gas phase) have been carried out on optimized model cations **B⁺, G⁺** and **R⁺** (see later in ESI for THF solution; for **G⁺** in THF solution see reference 4) to support the assignment of the low lying transitions (absorption and emission) in the complexes and silica based materials.

In THF solution (5×10^{-5} M, Fig. S12), complexes **B-R** exhibit intense absorptions at higher energies (<300 nm) due to spin allowed π-π* ligand centered transitions. The features at *ca.* 320 nm can be ascribed to ^{1}ILCT and ^{1}LL'CT (L= C^N; L'= PPETS, dasipy), with a certain ^{1}MLCT character for **G** and **R**. The weaker band observed at ca. 360 nm for **B** and **G** fits well with the lowest energy singlet transition computed, which is contributed by HOMO-LUMO. In both complexes, the HOMO is mainly centered on the metal and the phenyl groups of the cyclometalated ligands, while the LUMO is located on the pyridine groups. Therefore, this absorption has a mixed ^{1}ILCT/^{1}MLCT character. By contrast, for complex **R**, the low lying absorption at 384 nm is mainly ascribed to a mixed spin allowed ligand-to-ligand [C^N $\rightarrow$ N^N] and metal-to-ligand [Ir $\rightarrow$ N^N] charge transfer. Due to strong spin-orbit coupling (SOC) associated to Ir, all complexes show additional weak absorptions (412, 438 nm **B**; 424, 458 nm **G**; 467, 490 nm **R**) ascribed to spin forbidden (^{3}ILCT/^{3}MLCT **B**, **G**. ^{3}LL'CT/^{3}ML'CT 490nm; ^{3}ILCT/^{3}MLCT 467 nm **R**) transitions. These assignments are also in agreement with those found in the bibliography for related complexes.[4, 8] The diffuse reflectance UV-vis spectra (DRUV) of both the complexes (**B**, **G** and **R**) and the nanoparticle silica materials (**NP_B,G,R**) show similar features to those observed for the complexes in solution (see Fig. S13). The spectrum of the nanoparticles containing the three derivatives (**NP_W**) display characteristic features in the 200-400 nm range (246, 258, 268, 298, 311, 358 nm), and only the related material with a total nominal Ir concentration of 1wt.% (**NP_W_1wt%**, see Experimental) shows very weak absorptions at 468 and 498 nm.

The emissive properties of complex **G** have been already studied by our group.[4] Complexes **B** and **G** feature under photoexcitation at 365 nm, both in fluid and glassy

THF solution (Fig. S14 and S16), a long lived (0.92 μs, 298 K; 50.70 μs, 77K; **1**. 0.27 μs, 298 K; 44.00 μs, 77K; **2**) blue or green structured emission band (λ_{em} ~450, 480 nm **B**; ~460, 490 nm, **G**) attributed to a mixed ^{3}ILCT(C^N)/^{3}MLCT transition dominated by the π-π* contribution. As shown in Fig. S5,S6 for **B**, both SOMO and SOMO-1 orbitals and the spin-density distribution of the lowest optimized triplet state T_1 are mainly located on one cyclometalated ligand with a small contribution of the metal center (*ca.* 11% **B**, 16% **G**). The calculated electronic energies of the optimized lowest T_1 to S_0 (adiabatic transition; 504 nm **B**, 512 nm **G**) are close to the experimental values (450 nm **B**, 464 nm **G**), and the blue shift from **G** to **B** can be mainly attributed to stabilization of the HOMO (-6.40 eV **B** vs -6.1 eV **G**). Similar emission profile with a small red shift is observed for **B** in the solid state at low temperature (77 K), indicative of a mixed ^{3}ILCT/^{3}MLCT phosphorescence. However, at r.t. the emission profile becomes unstructured, pointing to an increase of the ^{3}MLCT contribution into the transition (Fig. S14). The photoluminescence quantum yield for complex **B** in THF solution is fourfold that of **G** (13.4% **1** vs 3.4% **2**), supporting the reduced non-radiative vibrations of C-F compared to C-H bonds. However, in the solid state the quantum yield of **G** (31.2 %) is higher than that found for **B** (23.5%), a feature that can be attributed to the significant AIE observed in the ppy complex **G**.[4] We have also explored the behavior of complex **B** blended in different amounts of poly(methylmethacrylate) (PMMA). As observed in Table S7 and Fig. S15, the luminescence quantum yield is not enhanced by increasing the concentration of **B** in PMMA, showing the best efficiency in this media at a concentration of 10%. As expected, at the lower concentration of the chromophore, the structured emission characteristic of the fluid media is observed, while the unstructured emission noticed in the solid state appears at concentrations up to 70%.

Upon excitation from 420 – 470 nm, complex **R** displays in THF solution at r.t. a broad unstructured red emission at 610 nm, which is notably blue-shifted and slightly structured at 77 K (570 nm, Fig. S17). Based on previous reports,[8a, 8b] and also supported by calculations on model cation **R$^+$**, the emission is mainly attributed to an admixture of ^{3}ML'CT(Ir → N^N)/^{3}LL'CT(ppy → N^N), having a remarkable ML'CT character (51%). The emission is red-shifted to that of previously reported in the literature for the parent complex [Ir(ppy)$_2$(bpy)]$^+$ (583 CH$_2$Cl$_2$;[9] 585 CH$_3$CN[10]), due to the presence of the two π-aceptor amide substituents in the target dasipy ligand, which decrease the energy gap in relation with the bipy ligand. Similar emission was observed in solid state (620

nm, 298 K; 610 nm, 77 K; Fig S17). The lower quantum yield measured in solid state (10.5%) in relation to solution (28.3%) could be indicative of quenching due to triplet-triplet annihilation.

All the nanoparticle material with a single complex (**NP_B,G,R**, nominal 0.2 wt.% of Ir) display long-lived unstructured emissions very similar (both λ_{em} and emission lifetimes, see Table S7) to those observed for the corresponding pure complexes (**B**, **G**, **R**) in the solid state at r.t. These emissions are also very similar to those observed for the corresponding previously hydrolyzed organometallic dots (**OD_B,G,R**), which have been measured in suspension directly from the reaction media (Table S7, Fig. 1). This supports the fact that the nanoparticles are designed by growth of the mesoporous silica around those emitting dots, which are formed by several molecules of each of the complexes, covalently bonded between them without any significant structural change relative to the pure complexes. Notably, these nanoparticles show quantum yield ranging from 15 to 20 %.

NP_W nanoparticles, which are assembled from organometallic dots obtained by the initial hydrolysis of a mixture of the three complexes to give a material with also a nominal iridium concentration of 0.2 wt.% (62.5 **B**: 32 **G**:5.5 **R** wt.%), exhibit a broad (full width at half maximum at ca. 6250 cm^{-1}) white emission with maxima at 490 and 595 nm (and a tail extending to 750 nm. Fig. 1) and a quantum yield of 20.5 % (λ_{exc} 390 nm). Not unexpected, the emission profile of this multiple emission is λ_{exc} dependent, with the lowest energy emission growing up when exciting at lower energies (Fig. S18). The excitation spectrum monitoring the lower emission energy (595 nm) shows an absorption maxima at 500 nm, thus indicating that the low energy chromophore is able to absorb energy at this wavelength. Moreover, a comparison between the emission lifetimes of **NP_W** monitored at 480 nm (0.57 μs), 510 nm (0.64 μs) and 595 (0.63 μs) with those obtained monitoring **NP_B** (0.99 μs), **NP_G** (0.89 μs) and **NP_R** (0.12 μs) at the respective wavelengths reveals a slight decrease in the blue and green emitter and a clear enhanced in the red one.[11] As expected, **OD_W** dots, measured in suspension directly from the reaction media, display emission features quite similar to those described for the **NP_W** nanoparticles. As observed in Table S7 (Fig. 1), these particles also show a broad (full width at half maximum at ca. 6450 cm^{-1}) white emission with maxima at 490 and 615 nm, with a λ_{exc} dependent profile (Fig. S18). Also in this case, the differences between the emission lifetimes of **OD_W** monitored at 480 nm (0.40 μs), 510 nm (0.57

µs) and 600 (0.50 µs), and those obtained monitoring **OD_B** (1.18 µs), **OD_G** (0.75 µs) and **OD_R** (0.14 µs) at the respective wavelengths show the same trend as for the nanoparticle **NP**.

For comparative purposes, we also mixed the appropriate amounts of nanoparticles **NP_B**, **NP_G** and **NP_R** to obtain a homogeneous mixture with the same proportion of chromophores than in **NP_W** (62.5 **B**:32 **G**:5.5 **R** wt.%). As is shown in Fig S19, the mixture performs a weaker broad emission with a different profile to that observed for **NP_W,** where the low energy maximum (ca. 600 nm) is lost, likely due to some degree of reabsorption. All these facts point to the occurrence of a certain degree of *energy transferenc*e from the blue and green chromophores to the red one in **NP_W** and **OD_W**, and could explain the high contribution of the low energy emission in spite of the small relative amount of complex **R** in the final mixture of the three derivatives (5.5 wt.%). Energy transfer is a short distance range process (up to 8 nm)[12] which cannot happen in the homogeneous mixture of **NP_B**,**G**,**R**, where each single emitter is localized inside silica nanoparticles between 50-70 nm of diameter. By contrast, in **NP_W** the three chromophores are well integrated into the nanoparticle and close in their adequate proportions. Moreover, a similar behavior is observed by blending adequate volumes of the water/ethanol suspensions of **OD_B**, **OD_G** and **OD_R**. This mixture also shows a weaker emission, where the low energy maximum (ca. 600 nm) strongly diminishes its intensity, being lost by excitation at 360 nm (Fig. S19).

Table S6. Absorption data in solution (THF, 5 x 10^{-5} M) and solid state of complexes **B**, **G** and **R** and of their hybrid organometallo-silica nanoparticles (**NP**).

Sample	λ_{abs}/ nm (ε/ M^{-1} L^{-1})
[Ir(dfppy)$_2$(PPETS)$_2$]PF$_6$ (**B**)	258 (44.8), 310 (18.2), 350 (6.0), 412 (0.1), 438 (0.05) ***THF*** 241, 279, 296, 316, 332, 350, 410, 440 ***Solid***
NP_B	230, 240, 260, 297, 312, 350 ***Solid***
[Ir(ppy)$_2$(PPETS)$_2$]OTf (**G**)[a)]	242 (22.1), 270 (13.8), 320 (5.5), 366 (2.1), 424 (0.3), 458 (0.02) ***THF*** 221, 248, 267, 321, 366, 420, 452 ***Solid***
NP_G	240, 264, 314, 362 ***Solid***
[Ir(ppy)$_2$(dasipy)$_2$]OTf (**R**)	255 (61.7), 270 (78.2), 285 (67.7), 323 (34.2), 360 (16.3), 384 (14.5), 467 (2.1), 490 (1.6) ***THF*** 223, 258, 276, 297, 320, 380, 468, 493 ***Solid***
NP_R	224, 238, 272, 294, 310, 372, 467, 494 ***Solid***
NP_W	246, 258, 268, 298, 311, 358 ***Solid***

a) Data obtained from reference 4 of this Supporting Information

Table S7. Experimental and calculated emission data of complexes **B**, **G** and **R** in solid state and solution (THF or CH_2Cl_2, 5 x 10^{-4} M) and of their hybrid organometallo-silica nanoparticles (**NP**) and dots (**OD**).

Sample	Medium (T/K)	λ_{em}/ nm (λ_{ec}/nm)	$\Delta E(T_1\text{-}S_0)$ (nm)	$\tau/\mu s$[a]	ϕ/%
B	Solid (298)	480	506	1.55	23.5
	Solid (77)	457, 483$_{max}$, 515$_{sh}$		28.42	
	THF (298)	450, 480$_{max}$, 510$_{sh}$	504	0.92	13.4
	THF (77)	450, 475$_{max}$, 505$_{sh}$		50.71	
1% PMMA	Solid (298)	450, 477$_{max}$			36.5
10% PMMA	Solid (298)	458, 477$_{max}$			40.9
50% PMMA	Solid (298)	462, 477$_{max}$			32.7
70% PMMA	Solid (298)	477			23.5
NP_B	Solid (298)	488		0.99	19.6 (365); 15.4 (390)
OD_B	*Sol*[b] (298)	485		1.18	17.5 (365); 11.7 (390)
G[c]	Solid (298)	512	524	0.97	31.2
	Solid (77)	463, 480, 504$_{max}$, 530$_{sh}$		15.80	
	THF (298)	464, 494$_{max}$, 520$_{sh}$	512	0.27	3.4
	THF (77)	460$_{max}$, 493, 519$_{sh}$		44.00	
NP_G	Solid (298)	508		0.89	15.7 (365); 13.7 (390)
OD_G	*Sol*[b] (298)	500		0.75	10.0 (365); 8.5 (390)
R	Solid (298)	620	614	0.13	13.1 (390); 16.5 (480)
	Solid (77)	610$_{max}$, 640$_{sh}$		1.04	
	THF (298)	610	598	0.20	28.3
	THF (77)	570$_{max}$, 600$_{sh}$		14.30	
NP_R	Solid (298)	630		0.12	8.7 (390); 10.5 (480)
OD_R	*Sol*[b] (298)	625		0.14	9.2 (390); 6.6 (480)
NP_W	Solid (298)	490, 595[d] (390)		0.57 (480) 0.64 (510) 0.63 (595)	26.7 (365); 20.5 (390)
OD_W	*Sol*[b] (298)	490, 615 (390)		0.40 (480) 0.57 (510) 0.50 (600)	10.6 (365); 9.1 (390)

a) Solid state emissions lifetimes calculated as average of a bi-exponential decay. Solutions and glasses calculated as mono-exponential decay. b) Measured directly from the reaction media. c) Data obtained from reference 4 of this Supporting Information. d) Tail extending to 750 nm.
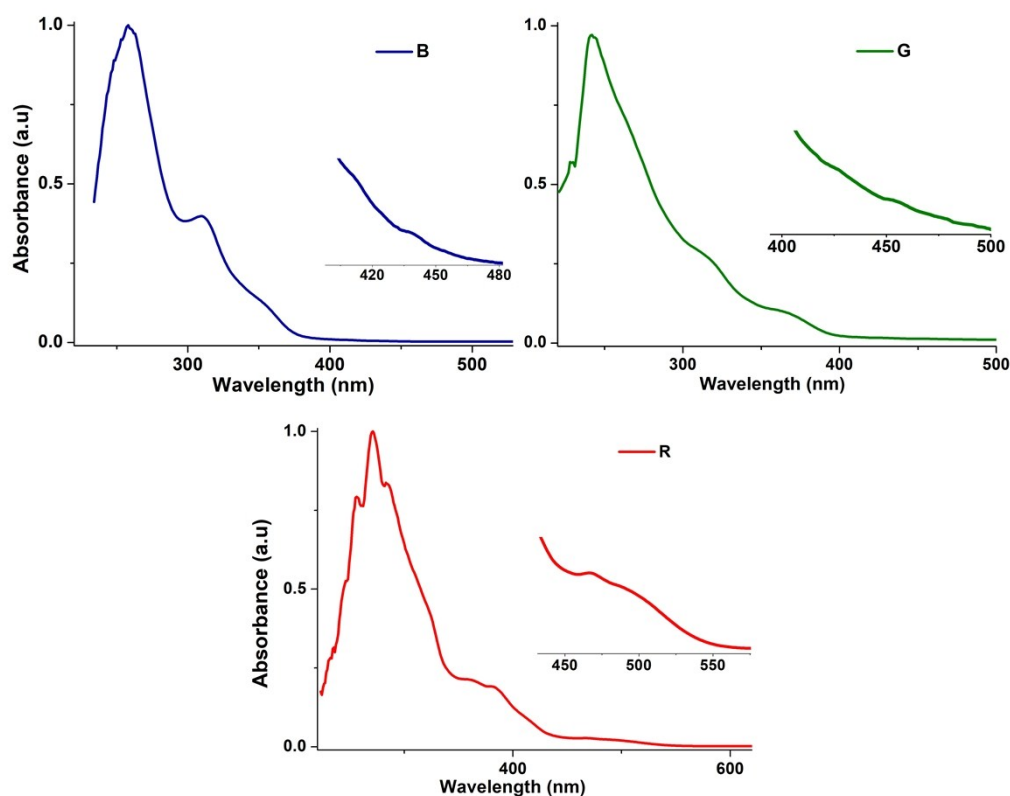Data measured with λ_{ex} at 365 nm for **B** and **G** and at 420-470 nm for **R**.

Figure S12. Absorption spectra of complexes **B**, **G** and **R** in THF solution (5 x 10^{-5} M).
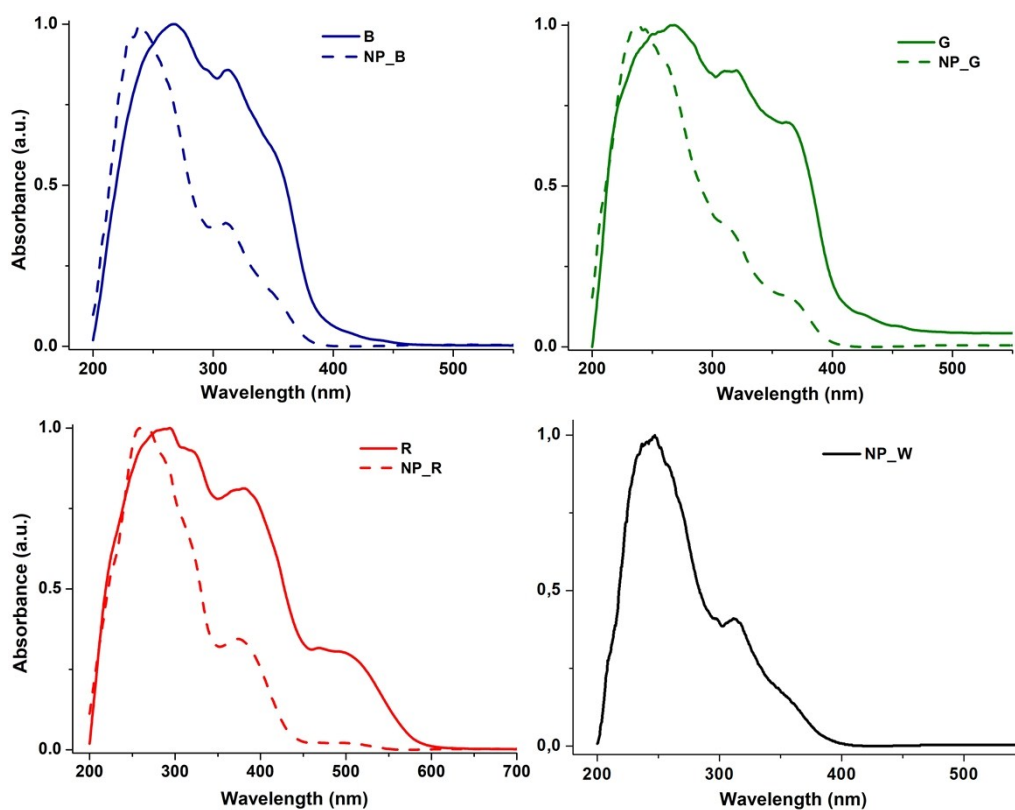

Figure S13. Solid state DRUV spectra of complexes **B**, **G** and **R** and the monochromatic-**NP_B**,**G**,**R** and the white-emitting **NP_W** organometallo-silica nanoparticles.
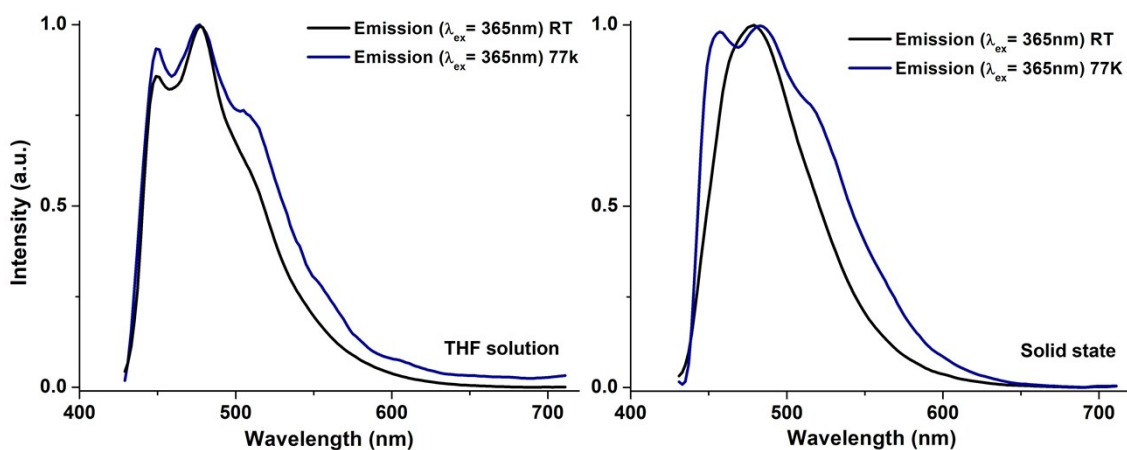
Figure S14. Emission spectra of complex **B** in THF solution (left, 5 x 10^{-4} M) and in the solid state (right), at room temperature and at 77K.
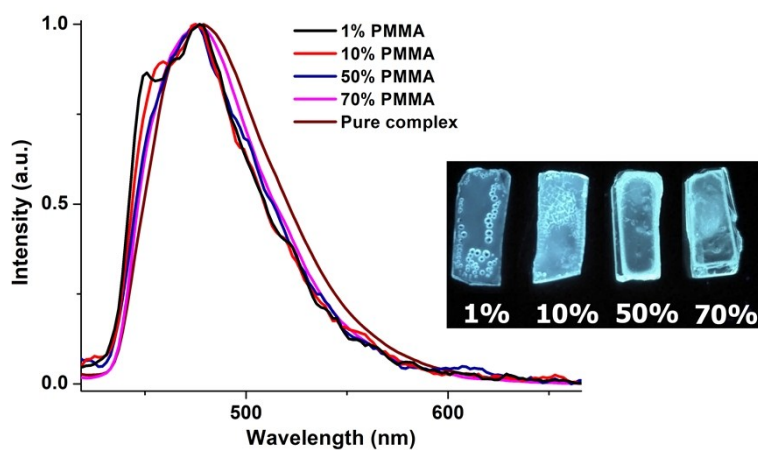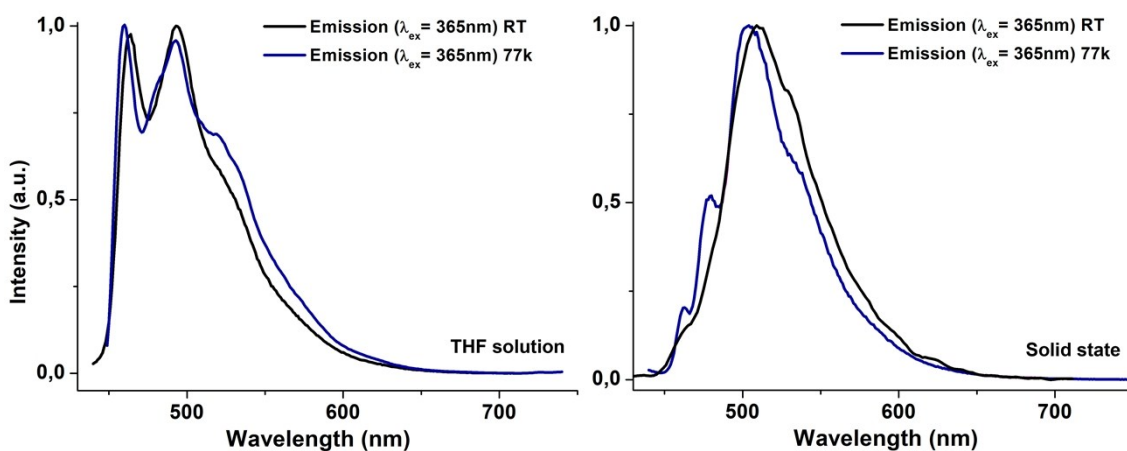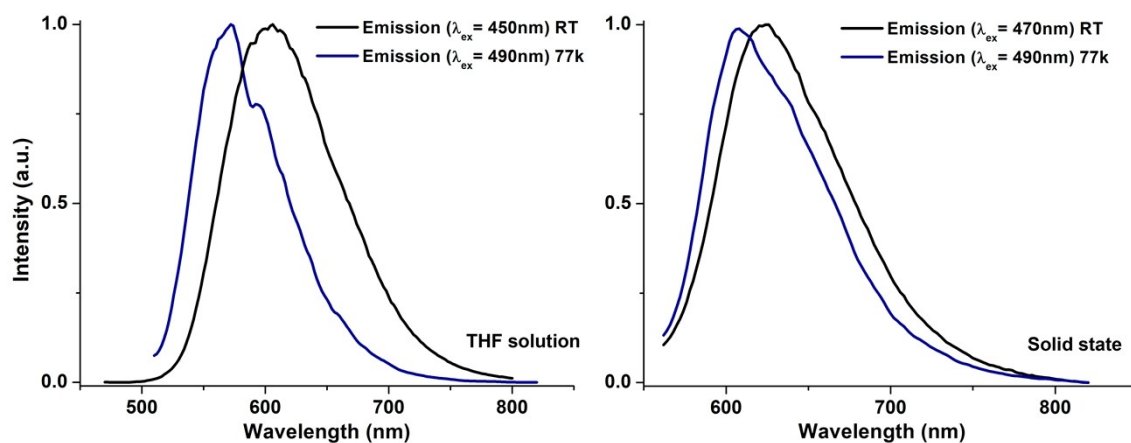

Figure S15. Normalized emission spectra of different concentrations of complex **B** in PMMA at room temperature.

Figure S16. Emission spectra of complex **G** in THF solution (left, 5 x 10^{-4} M) and in the solid state (right), at room temperature and at 77K.

Figure S17. Emission spectra of complex **R** in THF solution (left, 5 x 10⁻⁴ M) and in the solid state (right), at room temperature and at 77K.
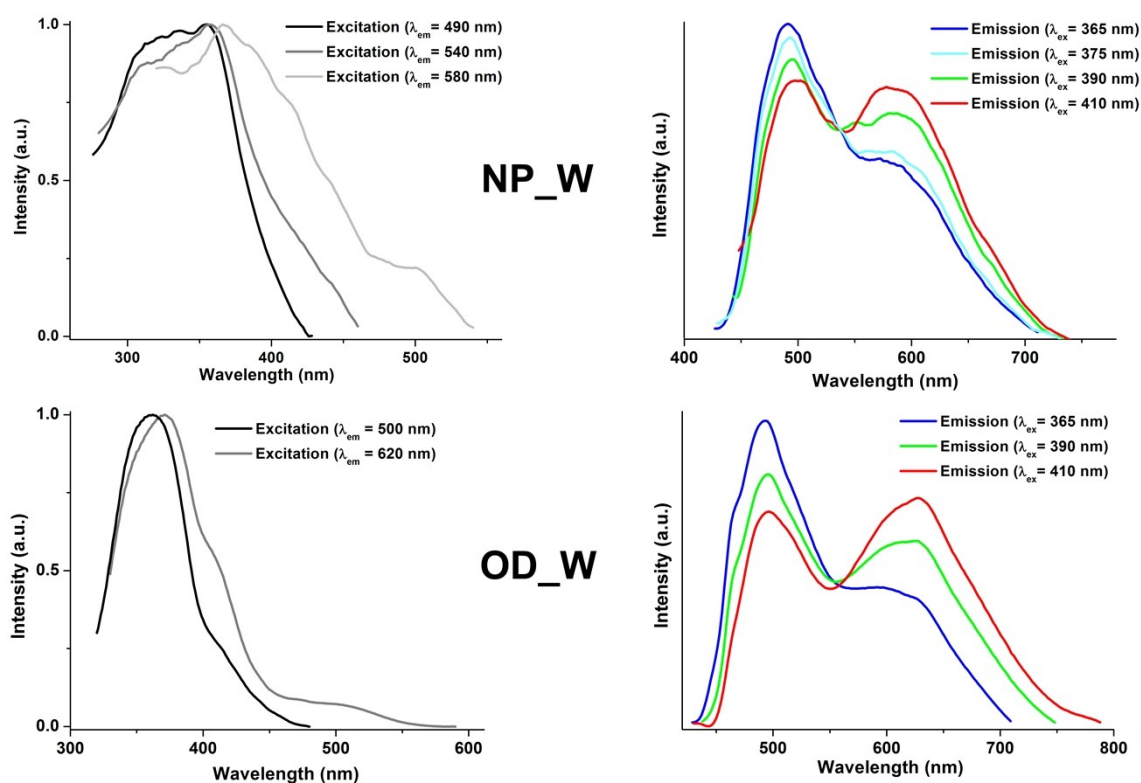
Figure S18. Excitation (left) and emission (right) spectra of the white-emitting nanoparticles **NP_W** (up, solid state) and organometallic dots **OD_W** (down, suspension from the reaction media) monitored at different λ.
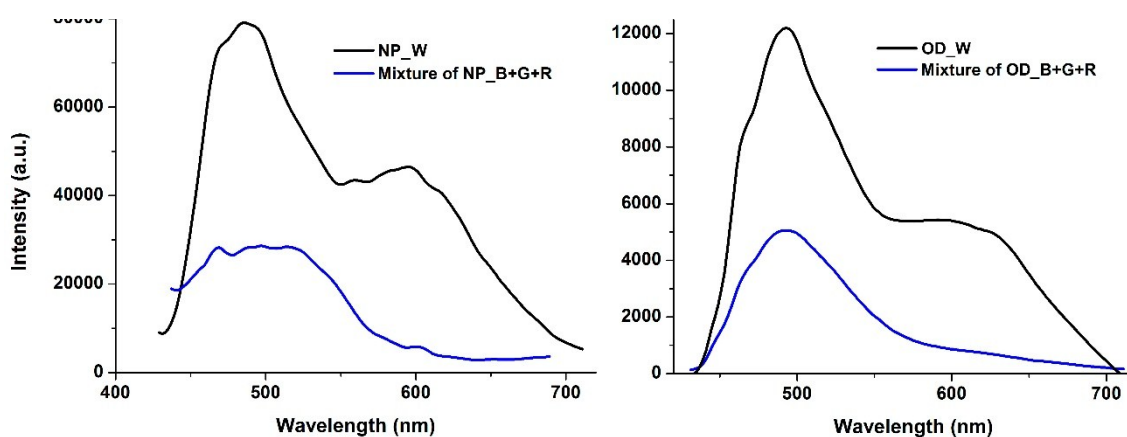
Figure S19. Emission spectra of the three-in-one white-emitting nanoparticles **NP_W** (left, solid state) and organometallic dots **OD_W** (right, suspension from the reaction media) compared with a mixture of the appropriate amount of solid monochromatic nanoparticles (**NP_B**, **NP_G** and **NP_R**) or volumes of the water/ethanol reaction media of the monochromatic dots (**OD_B**, **OD_G** and **OD_R**), respectively, to get the same proportion of chromophores (62.5 **B**:32 **G**:5.5 **R** wt.%; λ_{exc} 360nm).

6. Photostability measurements
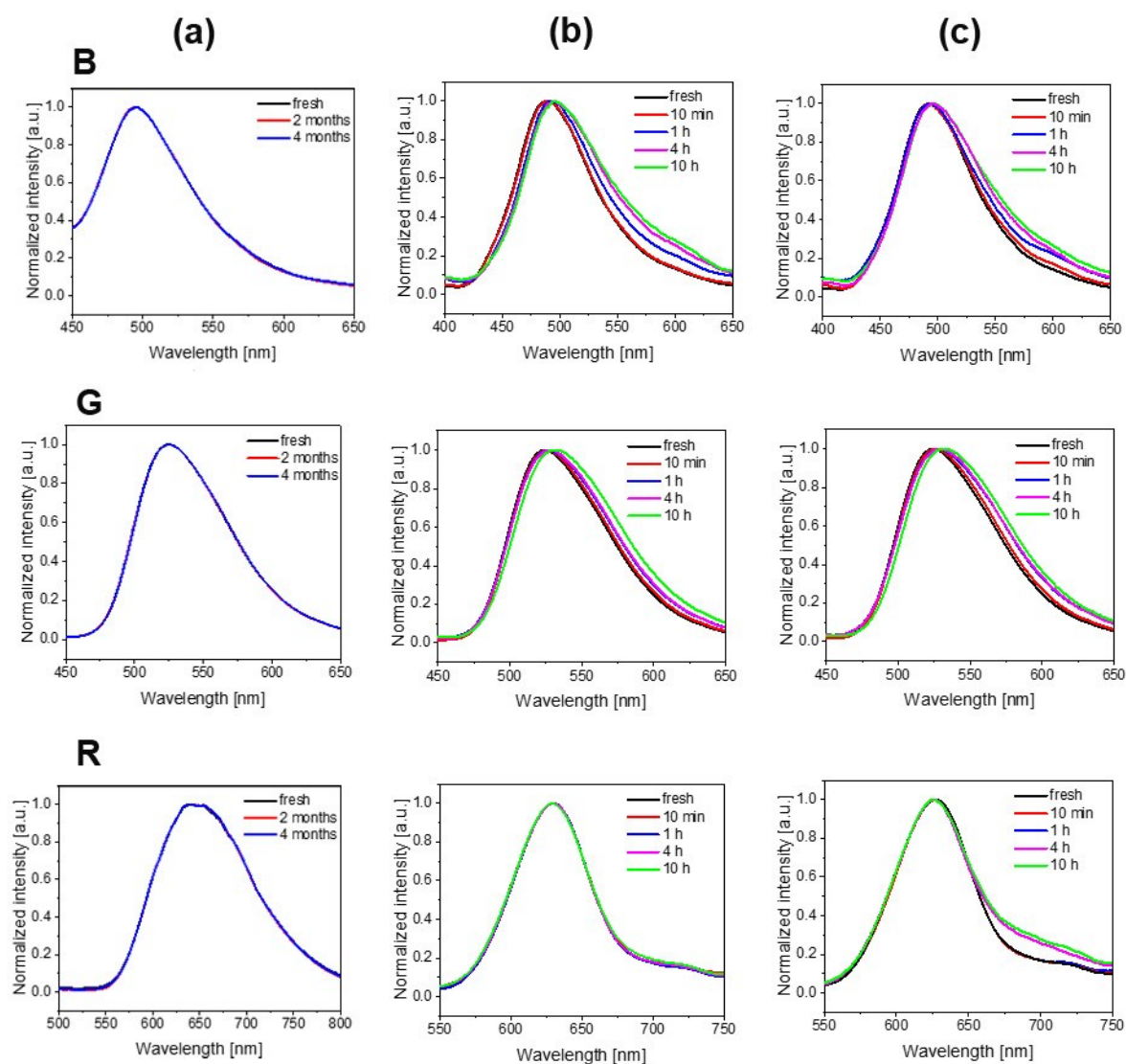
Figure S20. Changes in the emission spectra (λ_{exc} 400 nm LED) of **OC**-rubbers based on the organometallic complexes (**B**, **G**, **R**) over time under ambient storage conditions (a), under UV irradiation (302 nm; 8 W) at room temperature (b), and under UV irradiation (302 nm; 8 W) at 70ºC.
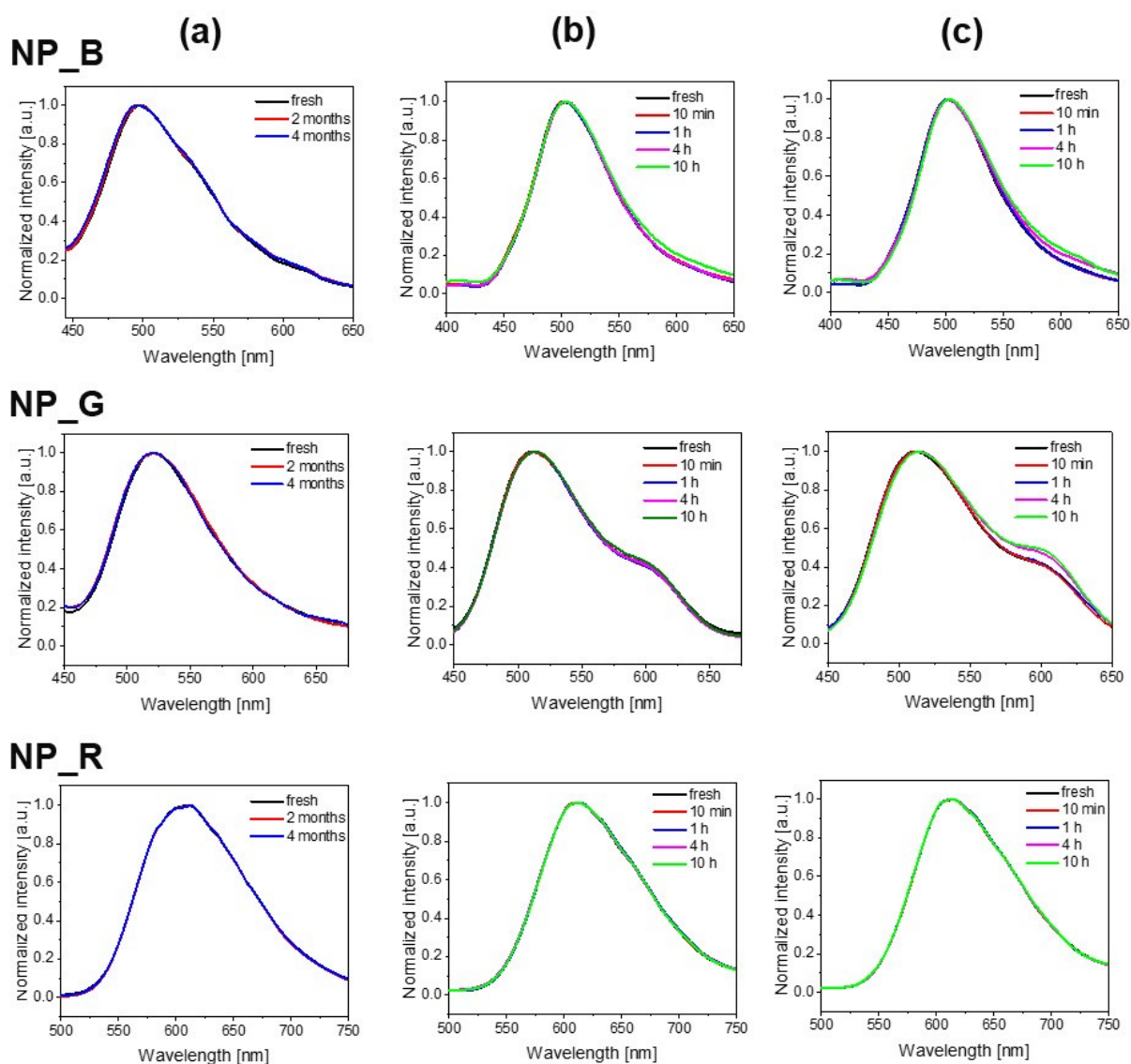
Figure S21. Changes in the emission spectra (λ_{exc} 400 nm LED) of **NP**-rubbers based on the monochromatic organometallo-silica nanoparticles (**NP_B**, **NP_G**, **NP_R**) over time under ambient storage conditions (a), under UV irradiation (302 nm; 8 W) at room temperature (b), and under UV irradiation (302 nm; 8 W) at 70ºC.

7. Fabrication and characterization of WHLEDs

Preparation and characterization of gels and rubber-like materials

As a first step, an acetonitrile solution with the different complexes or **NP**s was added to a 6:1 mixture of branched and linear poly(ethylene oxide) compounds, that is, trimethylolpropane ethoxylate (TMPE) with Mn of 450 mol/g and linear poly(ethylene oxide) (l-PEO) with Mn of 5×10^6 mol/g, respectively. Both materials were purchased from Sigma Aldrich and used as received. In the range of concentration studied (1-5 mg/mL), the formation of the gels and the final rubber-like materials are independent of both the complexes or NPs added amount. By using acetonitrile solutions containing 1mg/mL of the corresponding complexes, the optimized mixture of Ir complex:TMPE:l-PEO, in a mass ratio of 1:40:6.7, is best described as an initial suspension, which becomes a gel upon strong stirring (1500 rpm) under ambient conditions overnight. The doctor-blading was performed using a rectangular stamp of a thickness of 50 μm that was placed onto the support. They can also be applied onto 3D substrates by introducing them into the gels. Subsequently, the films were introduced into a vacuum station under 1-10 mbar for less than 1 h. The final materials are best described as rubber-like material (see Fig. 2), which are easily peeled off from the substrate with tweezers, and can be transferred to another substrate. The thickness of the rubber-material can be controlled either by the thickness of the stamp or by the subsequent deposition of one layer on top of another with an excellent adhesion.

Fabrication and characterization of the HLEDs

The UV-LED (400 nm) was purchased from WINGER®. The preparation of the HLEDs concerns a two steps procedure. Firstly, the gels are deposited onto the LED, wetting the surface completely. Secondly, the coated LED is transferred to the vacuum chamber under 1-10 mbar for less than 1 h. This procedure is repeated to enhance the light down-conversion efficiency of the HLED. The optimized thickness of the coating for devices is approximately 1-1.5 mm.

The HLEDs were characterized using a Keithley 2400 as a current source, while the luminous efficiency and changes of the electroluminescence spectrum were monitored by using Avantes spectrophotometer (Avaspec-ULS2048L-USB2) in conjunction with an integrating sphere Avasphere 30-Irrad. At the applied driving conditions, the top temperature of the LED did not significantly change from r.t. values over time.
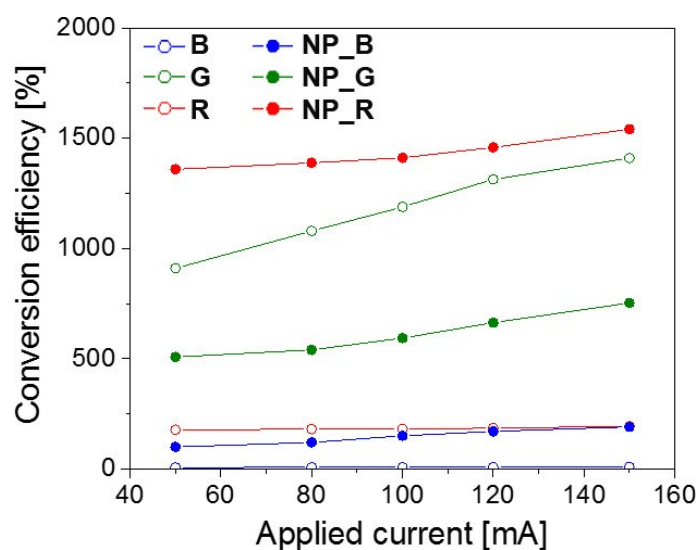
Figure S22. Conversion efficiency (η_{con}) versus applied currents for down-converting coatings prepared with OC- and NP-rubbers.
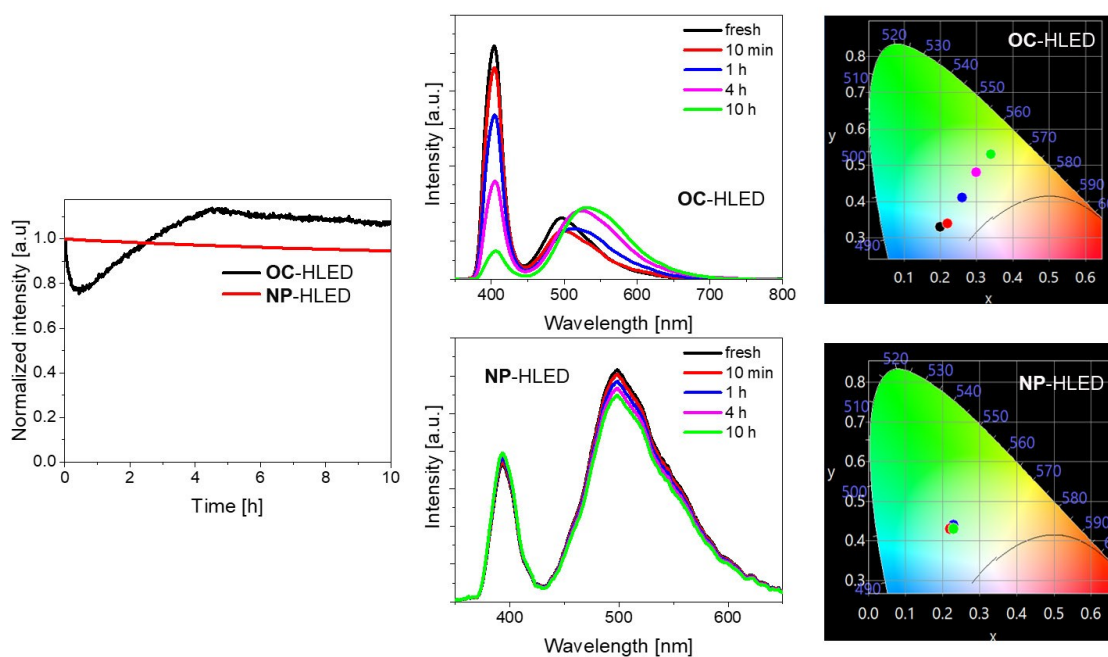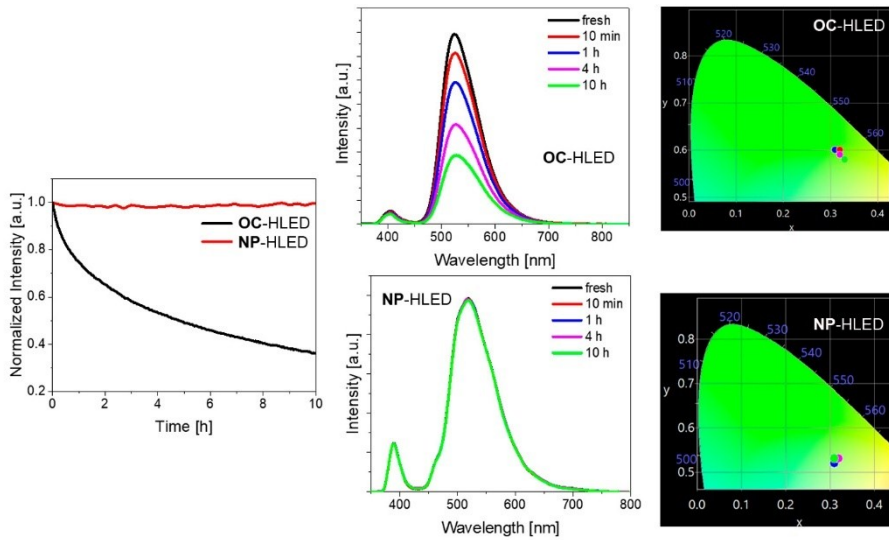

Figure S23. Changes in the intensity of the down-conversion band (left), spectrum shape (central), and x/y CIE color coordinates (right) of blue-emitting **OC**-HLEDs (top, based on **B**) and **NP**-HLEDs (bottom, based on **NP_B**) over time upon applying a constant current of 150 mA.
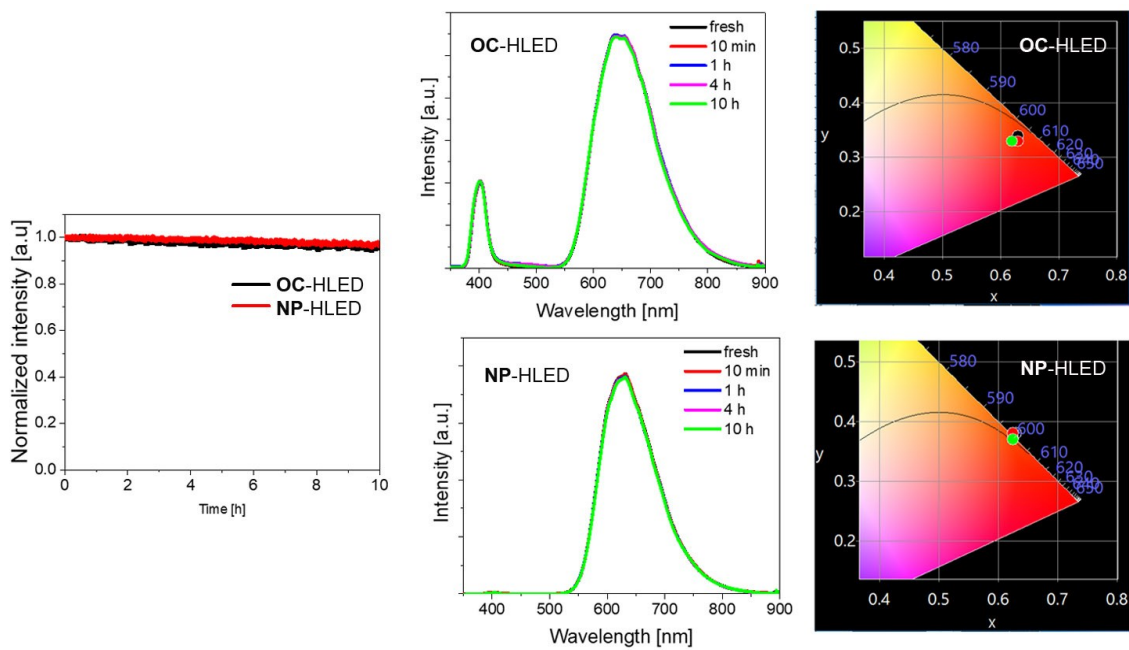
Figure S24. Changes in the intensity of the down-conversion band (left), spectrum shape (central), and x/y CIE color coordinates (right) of green-emitting **OC**-HLEDs (top, based on **G**) and **NP**-HLEDs (bottom, based on **NP_G**) over time upon applying a constant current of 150 mA

Figure S25. Changes in the intensity of the down-conversion band (left), spectrum shape (central), and x/y CIE color coordinates (right) of red-emitting **OC**-HLEDs (top, based on **R**) and **NP**-HLEDs (bottom, based on **NP_R**) over time upon applying a constant current of 150 mA.
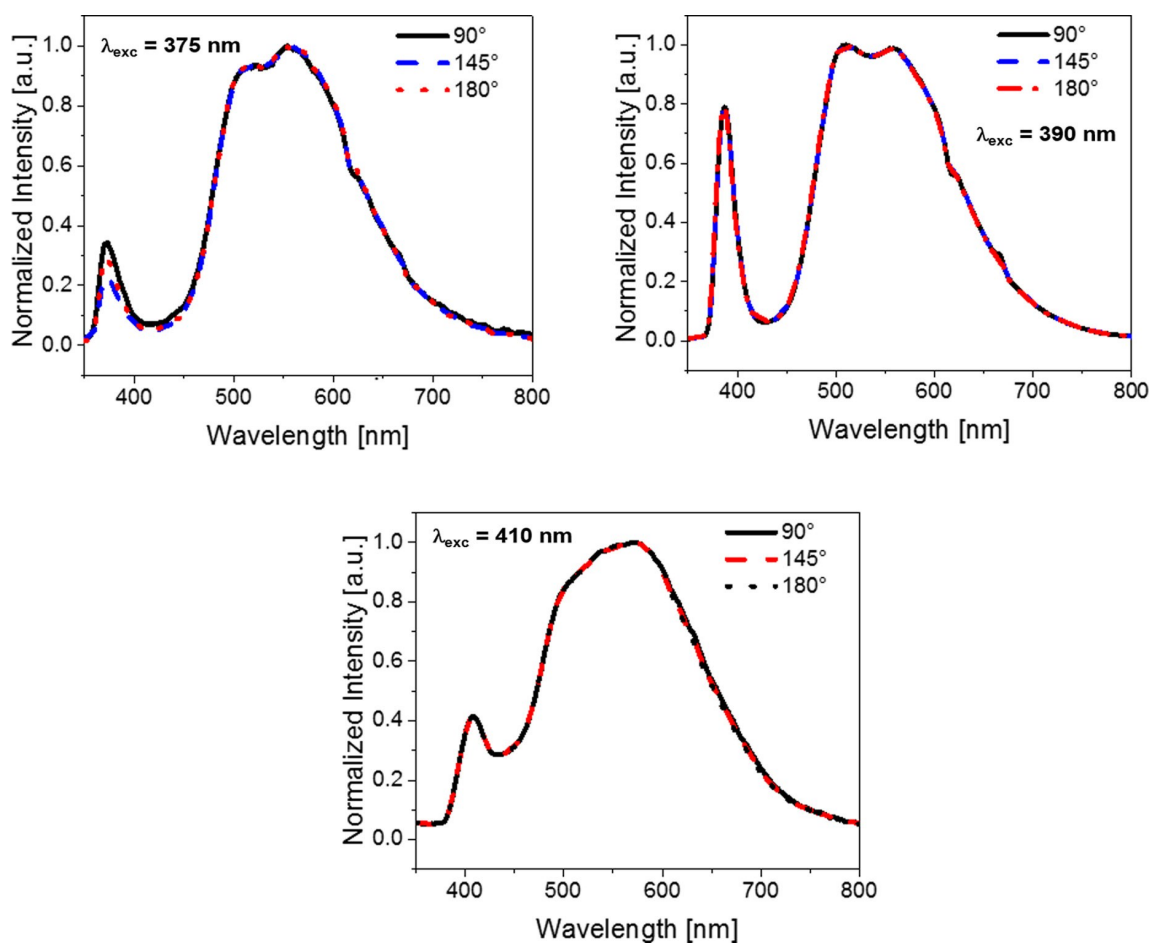
Figure S26. Normalized electroluminescence spectra of **NP**-HWLED with **single-component** down-converting coating (based on **NP_W**) recorded at different angles (λ_{exc} = 375 nm, top left; 390 nm, top right; 410 nm, bottom).

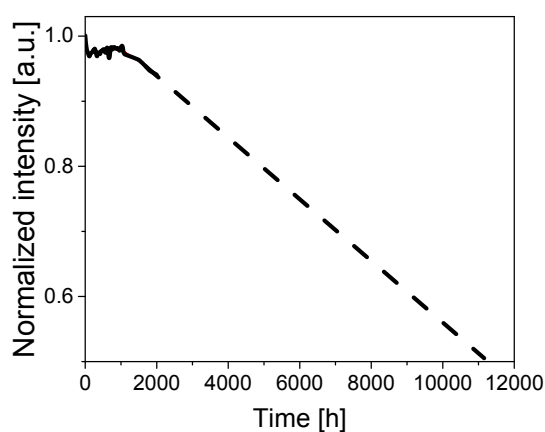**Figure S27**. Extrapolated stability values of **NP**-HWLED with single-component down-converting coating (based on **NP_W**) over time under applied constant current of 150 mA.
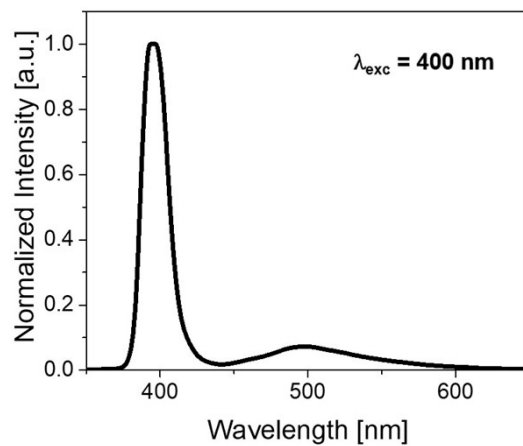
Figure S28. Normalized electroluminescence spectra of **NP**-WHLED with **multi-component** down-converting NPs (based on a mixture of **NP_B**, **NP_G** and **NP_R**) using the same chromophore concentration than the single-component NPs (λ_{exc} = 400 nm).

8. References

1. B. Schmid, F. O. Garces and R. J. Watts, *Inorg. Chem.*, 1994, **33**, 9-14.
2. Y. Zhou, W. Li, Y. Liu and M. Zhou, *ChemPlusChem*, 2013, **78**, 413-418.
3. G. M. Greenway, A. Greenwood, P. Watts and C. Wiles, *Chem. Commun.*, 2006, 85-87.
4. C. Ezquerro, A. E. Sepulveda, A. Grau-Atienza, E. Serrano, E. Lalinde, J. R. Berenguer and J. Garcia-Martinez, *J. Mater. Chem. C*, 2017, **5**, 9721-9732.
5. M. J. Frisch, G. W. Trucks, H. B. Schlegel, G. E. Scuseria, M. A. Robb, J. R. Cheeseman, G. Scalmani, V. Barone, B. Mennucci, G. A. Petersson, H. Nakatsuji, M. Caricato, X. Li, H. P. Hratchian, A. F. Izmaylov, J. Bloino, G. Zheng, J. L. Sonnenberg, M. Hada, M. Ehara, K. Toyota, R. Fukuda, J. Hasegawa, M. Ishida, T. Nakajima, Y. Honda, O. Kitao, H. Nakai, T. Vreven, J. A. Montgomery, J. E. Peralta, F. Ogliaro, M. Bearpark, J. J. Heyd, E. Brothers, K. N. Kudin, V. N. Staroverov, R. Kobayashi, J. Normand, K. Raghavachari, A. Rendell, J. C. Burant, S. S. Iyengar, J. Tomasi, M. Cossi, N. Rega, J. M. Millam, M. Klene, J. E. Knox, J. B. Cross, V. Bakken, C. Adamo, J. Jaramillo, R. Gomperts, R. E. Stratmann, O. Yazyev, A. J. Austin, R. Cammi, C. Pomelli, J. W. Ochterski, R. L. Martin, K. Morokuma, V. G. Zakrzewski, G. A. Voth, P. Salvador, J. J. Dannenberg, S. Dapprich, A. D. Daniels, Farkas, J. B. Foresman, J. V. Ortiz, J. Cioslowski and D. J. Fox, *Gaussian 09, Revision B.01*, Gaussian, Inc., Wallingford CT, , 2009.
6. a) C. Lee, W. Yang and R. G. Parr, *Phys. Rev. B*, 1988, **37**, 785-789; b) A. D. Becke, *Phys. Rev. A*, 1988, **38**, 3098-3100; c) A. D. Becke, *J. Chem. Phys.*, 1993, **98**, 5648-5652.
7. N. M. O'Boyle, A. L. Tenderholt and K. M. Langner, *J. Comput. Chem.*, 2008, **29**, 839-845.
8. a) D. Ma, T. Tsuboi, Y. Qiu and L. Duan, *Adv. Mater.*, 2017, **29**, 1603253; b) A. F. Henwood and E. Zysman-Colman, *Chem. Commun.*, 2017, **53**, 807-826; c) A. F. Henwood and E. Zysman-Colman, *Top. Curr. Chem.*, 2016, **374**, 36.
9. L. L. Tinker, N. D. McDaniel, P. N. Curtin, C. K. Smith, M. J. Ireland and S. Bernhard, *Chem. Eur. J.*, 2007, **13**, 8726-8732.
10. R. D. Costa, E. Ortí, H. J. Bolink, S. Graber, S. Schaffner, M. Neuburger, C. E. Housecroft and E. C. Constable, *Adv. Funct. Mater.*, 2009, **19**, 3456-3463.
11. V. E. Pritchard, D. Rota Martir, E. Zysman-Colman and M. J. Hardie, *Chem. Eur. J.*, 2017, **23**, 8839-8849.
12. a) L. Grösch, Y. Lee, F. Hoffmann and M. Fröba, *Chem. Eur. J.*, 2015, **21**, 331-346; b) F. de Trindade, E. Triboni, B. Castanheira and S. Brochsztain, *J. Phys. Chem. C*, 2015, **119**, 26989-26998; c) G. Schwartz, S. Reineke, T. C. Rosenow, K. Walzer and K. Leo, *Adv. Func. Mater.*, 2009, **19**, 1319-1333.